NATIONAL ADVISORY COMMITTEE FOR AERONAUTICS

TECHNICAL NOTE 4268

DROPLET IMPINGEMENT AND INGESTION BY SUPERSONIC NOSE INLET IN SUBSONIC TUNNEL CONDITIONS

By Thomas F. Gelder

Lewis Flight Propulsion Laboratory
Cleveland, Ohio

Washington
May, 1958

NATIONAL ADVISORY COMMITTEE FOR AERONAUTICS

TECHNICAL NOTE 4268

DROPLET IMPINGEMENT AND INGESTION BY SUPERSONIC NOSE INLET IN SUBSONIC TUNNEL CONDITIONS

By Thomas F. Gelder

SUMMARY

The amount of water in cloud droplet form ingested by a full-scale supersonic nose inlet with conical centerbody was measured in the NACA Lewis icing tunnel. Local and total water impingement rates on the cowl and centerbody surfaces were also obtained. All measurements were made with a dye-tracer technique. The range of operating and meteorological conditions studied was: angles of attack of 0° and 4.2°, volume-median droplet diameters from about 11 to 20 microns, and ratios of inlet to free-stream velocity from about 0.4 to 1.8. Although the inlet was designed for supersonic (Mach 2.0) operation of the aircraft, the tunnel measurements were confined to a free-stream velocity of 156 knots (Mach 0.237). The data are extendable to other subsonic speeds and droplet sizes by dimensionless impingement parameters.

Impingement and ingestion efficiencies are functions of the ratio of inlet to free-stream velocity as well as droplet size. For the model and range of conditions studied, progressively increasing the inlet velocity ratio from less than to greater than 1.0 increased the centerbody impingement efficiency and shifted the cowl impingement region from the inner- to outer-cowl surfaces, respectively. The ratio of water ingested by the inlet plane to that contained in a free-stream tube of cross section equal to that at the inlet plane also increased with increasing inlet velocity ratio. Theoretically calculated values of inlet water (or droplet) ingestion are in good agreement with experiment for annular inlet configurations.

INTRODUCTION

The NACA has made numerous theoretical and experimental studies of the trajectories and impingement of cloud droplets on various bodies as well as on the ingestion of droplets by ducts and engine inlets (refs. 1 to 24). These data and those reported herein provide instantaneous values of droplet impingement and ingestion but do not consider the runback of impinged droplets. Knowledge of the droplet trajectories and/or local rates of impingement or ingestion by bodies is needed for a variety of applications; for example, (1) to assess the effects of liquid-water entrainment on the operation of air-breathing engines or instruments, (2) to determine the location and severity of ice formations and their effect on airplane and engine performance, and (3) to design icing protection equipment for various aircraft components.

The theoretical studies of droplet trajectories and impingement on airfoils, bodies of revolution, elbows, and inlet ducts were made with a differential analyzer (refs. 1 to 19). An experimental method developed at the NACA Lewis laboratory uses a dye-tracer technique to obtain impingement data directly and thus avoids the problem of calculating complex flow fields about arbitrary shapes. In the dye-tracer technique the quantity of dye collected locally on a blotter-wrapped body exposed to an airstream containing a dyed-water spray cloud is colorimetrically determined and converted to local impingement rate. Dye-tracer results are reported for cylinders, airfoils, and bodies of revolution in references 21 to 24. Good agreement between the differential-analyzer and dye-tracer impingement results has generally been obtained through comparative studies of similar body shapes.

4704

The present investigation provides local and total water impingement rates on the cowl and centerbody surfaces of a full-scale supersonic nose inlet and the rate of water ingestion by the inlet annulus. The inlet studied had a translating conical centerbody (fully retracted herein) and was designed for Mach 2.0. Studies were conducted with the inlet at angles of attack of 0° and 4.2° and over a range of ratios of inlet to free-stream velocity from about 0.4 to 1.8 in a subsonic free stream. This range of inlet velocity ratios was arbitrarily selected to cover the ratios most used in flight. These data were obtained in the NACA Lewis icing tunnel by using the dye-tracer technique.

APPARATUS

Model and Installation

A front view of the supersonic-nose-inlet model installed in the 6- by 9-foot test section of the Lewis icing tunnel is shown in figure 1. The over-all length of the installation was about 19 feet, with a main support pedestal located near the midpoint. Additional support was provided by an A-frame just aft of the inlet lips.

The conical centerbody was supported by three equally spaced sweptback struts mounted from the outer shell or cowling, as indicated by the schematic drawing of the inlet and afterbody in figure 2(a). The inlet (first 7 ft of model) was a full-scale prototype with the external cowling modified somewhat aft of about 2 feet from the inlet lips. The model afterbody contained ejector nozzles and ducting to simulate the pumping action of an engine compressor. The over-all top view of figure 2(a) shows the inlet at an angle of attack of 4.2°. Because of the model and tunnel size, only the forward half of the installation was at angle of attack relative to the free stream. A transition section was inserted between the inlet and afterbody to effect the 4.2° angle of attack in a plane parallel to the 9-foot width of the tunnel floor; thus, the actual nacelle top was rotated 90° from the tunnel top position (see fig. 2(a)).

The nacelle stations noted on figure 2(a) are referenced to an arbitrary transverse plane 1.9 inches upstream of the leading edge of the inlet lips. The tip of the conical centerbody (25° half-angle) is $5\frac{1}{2}$ inches upstream of station 0. The conical centerbody fairs into a cylindrical section at station 20. At the end of the straight cylindrical section (station 35), the centerbody narrows to a smaller cylindrical section that ends at the instrumented compressor-face station 85. A conical tailpiece closes the centerbody contour. Aft of this tailpiece is the transition section for angle-of-attack simulation. The 19 ejector nozzles are located between stations 110 and 129, and a butterfly valve is at station 201.

For these dye impingement studies, two pieces of bar stock (hereinafter called sabers) were inserted through the cowling to span the flow annulus at nacelle stations 6.7 (forward saber) and 25.5 (rear saber). The forward saber was $\frac{1}{8}$ by $\frac{1}{2}$ by $8\frac{1}{2}$ inches; the rear saber was $\frac{1}{8}$ by $\frac{1}{2}$ by $5\frac{1}{2}$ inches. The front-view schematic drawing of the inlet shown in figure 2(a) indicates the clock positions (as mounted in the tunnel) of the two sabers as well as the three centerbody support struts. The rear saber was used primarily for a check on the forward saber.

Figure 2(b) presents the annular flow areas within the inlet from the cowl-lip station 1.9 to the compressor-face station 85. These flow areas account for the presence of the centerbody struts and are calculated on the assumption that the airflow through the annulus has the vector direction of the dashed line in figure 2(b). This dashed line represents the locus of the mean radius at each station. Mean radius is defined on figure 2(b). All symbols are defined in appendix A.

Local body radius and surface distance of the inlet components as a function of nacelle station are presented in figure 2(c).

The 19 ejector nozzles, in the symmetrical array shown in figure 2(a), received primary air from a 12-inch high-pressure supply line. This air line, brought through the tunnel floor and into a ring manifold formed by the inner and outer walls of the ejector duct, also served as the main support pedestal for the model. Flow of high-pressure air through the ejector nozzles was required in order to achieve inlet velocity ratios greater than 1.0. Although the ejector and the butterfly valve are both shown for convenience of illustration in figure 2(a), they were not used simultaneously.

Instrumentation

Part of the model instrumentation consisted of 17 centerbody and 20 inner-cowl flush wall static-pressure taps (fig. 3(a))[1]. The remaining pressure measurements were obtained from 16 rakes and 16 flush wall static taps at the simulated compressor-face station 85 (figs. 3(b) and (c)). The schematic drawing of the compressor-face instrumentation (fig. 3(c)) indicates that the five concentric rings of total-pressure tubes were located in equal annular flow areas. The eight pairs of flush wall static taps at the compressor face were spaced midway between adjacent rakes. In addition, one ring of eight stream static tubes was located at about the average radius of the flow annulus.

The compressor-face total pressures were measured by an integrating multitube manometer, and static pressures were measured by a conventional multitube manometer. Readings from these manometers were recorded photographically.

Spray System

The spray cloud was provided by eight air-water atomizing nozzles located in the quieting chamber upstream of the tunnel test section. The nozzles were positioned to provide a cloud that was relatively uniform in liquid-water content (less than ±10-percent variation from the average) and had essentially the same droplet size distribution throughout. The calibrated spray cloud at the center of the tunnel test section was about 2 feet wide (parallel to tunnel floor) and 1 foot high. The centerline of the inlet model was offset approximately 7 inches from the tunnel (also spray cloud) centerline so that an 180° sector of the inlet flow annulus was centered with respect to the spray cloud. For the impingement studies at angle of attack, the same 180° sector of the inlet was studied, first at an angle of attack of +4.2°, then at an angle of attack -4.2° (see view A-A of fig. 2(a)). The results thus obtained were equivalent to the windward and leeward surfaces at an angle of attack of 4.2°. Angles of attack greater than 4.2° could not be studied because of the limited size of the calibrated spray cloud.

Droplet size and liquid-water content were controlled by varying the pressures of the dyed water and air to the nozzles. The spray was turned on and off by fast-action solenoid valves; spray duration (nominally 2 to 12 sec) was controlled by an electric timer.

---

[1] The 30 outer-cowl static taps were not a part of the icing tunnel model; they were installed on a previous configuration tested by the model contractor. Data from these tests are presented subsequently for completeness.

The cloud total liquid-water content was obtained by collecting dye from the spray cloud in an aspirating device (a tube that draws in the cloud at free-stream conditions). The cloud droplet size and size distribution were determined by experimental and theoretical impingement on a 36.5-percent-thick symmetrical Joukowski airfoil. Details of the spray system and methods of determining the spray cloud properties are contained in references 21 and 22.

The three spray cloud conditions imposed on the inlet model are summarized as follows:

Spray condition	Liquid-water content, w_t, g/cu m	Volume-median[a] droplet diameter, d_{med}, microns	Maximum droplet diameter, d_{max}, microns
A	0.66	19.4	63
B	.51	16.7	44
C	.33	11.5	24

[a] Tunnel spray cloud droplet size distribution closely approximates a Langmuir "D" size distribution, which is typical of many natural icing clouds (refs. 22 and 25).

PROCEDURE

Dye-Tracer Technique

The mechanics of the dye-tracer technique including blotter mounting, tunnel conditioning, and blotter exposure were similar to those detailed in reference 22. The first 2 inches of the centerbody tip were enclosed with blotter paper preformed to a conical shape, which was followed by a 3/4-inch-wide strip extending past nacelle station 20. This centerbody strip was mounted along the three o'clock position (looking downstream into inlet, see fig. 2(a)). Blotter strips $2\frac{1}{2}$ inches wide were wrapped around the leading edge of the inlet cowl (on the three o'clock position) and extended along the inner- and outer-cowl surfaces to nacelle station 36. All blotters were both glued with rubber cement and taped to the model surface. Ribbons of blotter paper, $\frac{1}{8}$ by $1\frac{1}{2}$ inch (obtained from an accurately machined punch), were taped on the leading edge of the two sabers; five ribbons were placed end to end on the forward saber (nacelle station 6.7) and three ribbons on the rear saber (nacelle station 25.5).

The studies reported herein were conducted in a nearly saturated tunnel airstream at one nominal free-stream condition; namely, airspeed, 156 knots (Mach number 0.237); static pressure, 28.17 inches of mercury; and static air temperature, 56° F.

Inlet Model Operation

The desired inlet velocity ratio (ratio of the velocity at nacelle station 1.9 to the free-stream velocity) was obtained by the regulation of the pressure of the primary air to the 19 ejector nozzles or by the position of the butterfly valve. By assuming no loss in total pressure from the free stream to the inlet plane, the inlet velocity ratio was calculated from measurements of free-stream and compressor-face (nacelle station 85) static and total pressures.

The modes of inlet operation are summarized in the following table with inlet mass-flow ratio as well as inlet velocity ratio given for convenient reference. (The difference between the two ratios is due to compressibility.)

Angle of attack, α, deg	Mach number at nacelle station 85 (compressor face), M_{85}	Total-pressure recovery, P_{85}/P_0	Mass-flow ratio, m_i/m_0 (equal to area ratio A_0/A_i)	Inlet velocity ratio, V_i/V_0
0	0.092	0.999	0.397	0.387
	.159	.998	.678	.667
	.244	.995	1.016	1.017
	.323	.990	1.304	1.333
	.449	.968	1.674	1.781
4.2	0.096	0.999	0.414	0.404
	.162	.998	.690	.680
	.313	.992	1.270	1.294
	.446	.969	1.667	1.771

The three spray conditions (A, B, and C) previously discussed were imposed on each of the above modes of inlet operation. Several runs were made at each spray condition and inlet mode to establish repeatability of the data.

GENERAL CONSIDERATIONS OF INLET AIRFLOW AND IMPINGEMENT

For illustrative purposes, consider a thin-walled circular air inlet with no centerbody and a means of regulating airflow through the inlet (see sketch (a)). Also assume incompressible flow so that $V_i/V_0 = A_0/A_i$.

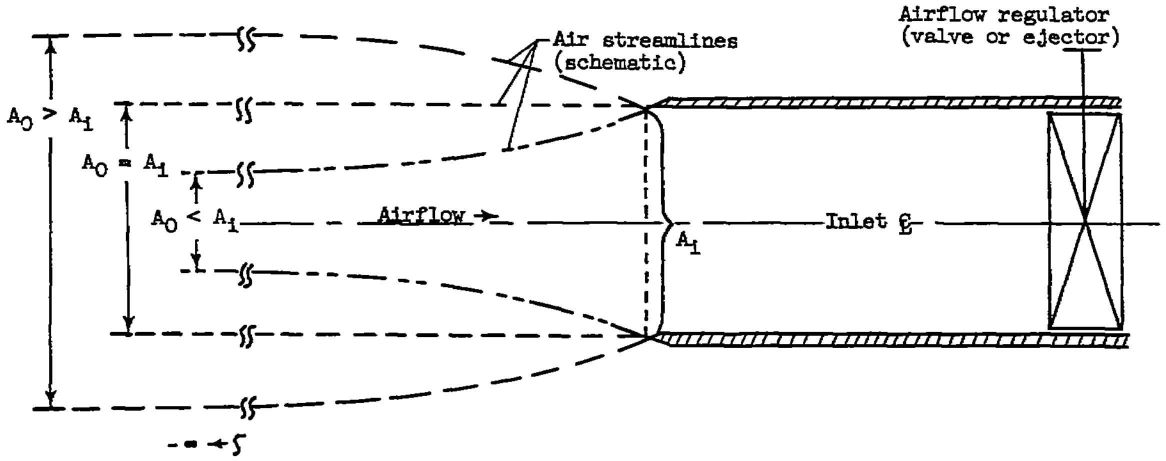

(a)

For an inlet velocity ratio V_i/V_0 of 1.0, the diameter of the inlet air stream tube is equal to the inlet diameter, that is, $A_0 = A_i$. For $V_i/V_0 > 1.0$, $A_i/A_0 < 1.0$; and for $V_i/V_0 < 1.0$, $A_i/A_0 > 1.0$.

Infinitely small droplets act like air particles, thus, the droplet trajectories are coincident with the air streamlines. For infinitely large droplets, the droplet trajectories are straight and parallel irrespective of the air streamlines or inlet velocity ratio. Finite droplet sizes have trajectories with a curvature intermediate to the extremes just discussed.

From these considerations at $V_i/V_0 < 1.0$ (see sketch (a)), the impingement on the inner walls of the inlet cowl could be considered as similar to that on the lower surface of an airfoil at angle of attack. Similarly for $V_i/V_0 > 1.0$, the cowl outer-wall impingement could be like that on the lower surface of an inclined airfoil.

Superimposing an inlet angle of attack on the above airflow patterns yields qualitative effects relative to those with the inlet at zero angle of attack as shown in sketch (b). For $V_i/V_0 < 1.0$, the leeward cowl is

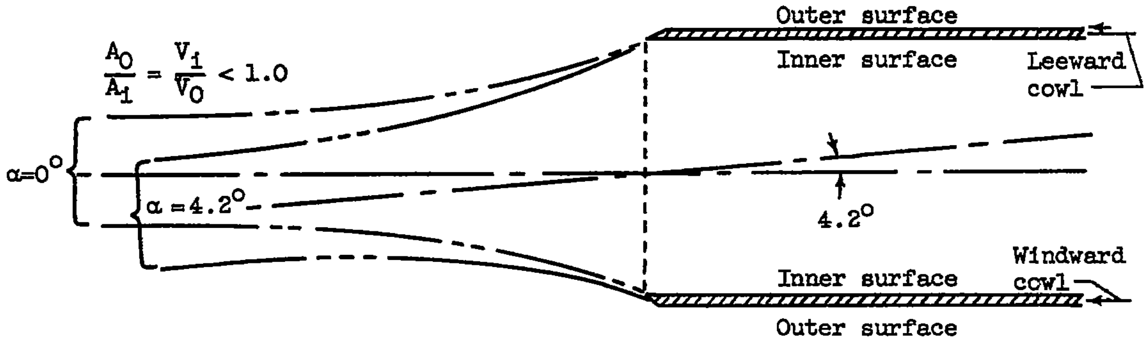

(b)

in effect at a higher angle of attack while the windward cowl is at a lower angle. Similarly, it can be shown that, for $V_i/V_0 > 1.0$, the windward cowl is at a higher angle while the leeward cowl is at a lower angle of attack.

For the inlet model studied (fig. 2) the presence and location of the conical centerbody do not alter any of the qualitative effects noted previously. However, these effects could be significantly different for annular inlets with large centerbody-to-inlet diameter ratios or inlets with part of the airflow annulus nonexistent (fuselage side ram scoops) or both. For such configurations and a particular inlet velocity ratio, the ratio of the inlet air stream-tube diameter to the inlet diameter would be reduced relative to that studied herein.

RESULTS AND DISCUSSION

As part of the impingement investigation herein, local surface velocity distributions over the inlet cowl and centerbody were obtained for the range of conditions studied. These velocity distributions are presented and discussed in appendix B.

Impingement Characteristics

The dye-tracer technique provides a direct local measurement of the pounds per hour of water impinging per square foot on any blotter-wrapped surface. The details of obtaining this local water impingement rate $\overline{W}_\beta$ are given in appendix C. Typical values of $\overline{W}_\beta$ as a function of cowl and centerbody surface distance s are presented in figure 4. These data are for the inlet at zero angle of attack, an inlet velocity ratio of 1.333, three spray conditions, and several repeat runs. From figure 4 the data indicate a repeatability better than ±10 percent. The mechanics of the blotter punching technique (see appendix C) precluded obtaining local water impingement rates on the centerbody ($\overline{W}_{\beta,cb}$) for $s_{cb} < 1/2$ inch. Thus, values of $\overline{W}_{\beta,cb}$ for s_{cb} between 0 and 1/2 inch are dotted on figure 4(a) with $\overline{W}_{\beta,cb,max}$ estimated from theoretical considerations. The exact value of $\overline{W}_{\beta,cb,max}$ is of minor importance, however, because it occurs on a negligible surface area.

By dividing the local impingement rate $\overline{W}_\beta$ by the rate available in the free stream, a local impingement efficiency $\overline{\beta}$ is defined (eq. (C1)). Hereafter, values of $\overline{\beta}$ (from faired plots of $\overline{W}_\beta$) are presented as a function of surface distance for the range of conditions studied.

<u>Local impingement efficiency $\overline{\beta}$</u>. - For the inlet model at zero angle of attack, $\overline{\beta}$ values as a function of s are presented in figure 5 for a range of inlet velocity ratios from 0.387 to 1.781. In figure 5, an increased inlet velocity ratio decreases inner cowl $\overline{\beta}$ ($\overline{\beta}_{ic}$) and increases outer cowl $\overline{\beta}$ ($\overline{\beta}_{oc}$), which supports the effective angle-of-attack reasoning previously discussed under GENERAL CONSIDERATIONS OF INLET AIRFLOW AND IMPINGEMENT. The high values of cowl $\overline{\beta}$ ($\overline{\beta}_c$) are concentrated within a few inches of the cowl leading edge for all values of inlet velocity ratio. Although the absolute value of $\overline{\beta}_{c,max}$ is difficult to determine, the trend is for an increase in $\overline{\beta}_{c,max}$ with increased values of V_i/V_0. For example, at spray condition A, $\overline{\beta}_{c,max}$ increases from about 0.5 to 0.7 with an increase of V_i/V_0 from 0.387 to 1.781. The location of $\overline{\beta}_{c,max}$ generally falls between the air stagnation point and the foremost point of the cowl; a similar trend was noted for airfoils in reference 22. At an inlet velocity ratio of 1.017 (fig. 5(c)) the $\overline{\beta}_c$ patterns are nearly symmetrical with insignificant impingement aft of 1 inch from the cowl leading edge.

The centerbody $\overline{\beta}$ values ($\overline{\beta}_{cb}$) of figure 5 increase with increasing values of V_i/V_0. One inch aft of the tip of the conical centerbody ($s_{cb} = 1$ in.) $\overline{\beta}_{cb}$ increases from 0.15 to 0.23 as V_i/V_0 increases from 0.387 to 1.781 under spray condition A. For all inlet velocity ratios $\overline{\beta}_{cb,max}$ occurs at the cone tip. As the inlet velocity ratio becomes greater than 1.0, the droplets entering the inlet plane through an annulus nearest the cowl lips are converging toward the centerbody. As a result, these converging trajectories create a concentration zone that increases impingement efficiencies toward the rear of the centerbody. This effect is most pronounced near an s_{cb} of 20 inches (nacelle station 13), where the diameter of the centerbody is large and has not as yet faired away into a straight cylindrical section (see fig. 2(c)).

For any given inlet velocity ratio, a reduction in volume-median droplet diameter d_{med} results in lower values of $\overline{\beta}$ for both cowl and centerbody. For example, at a V_i/V_0 of 1.017 (fig. 5(c)) and an s_{cb} of 1 inch, $\overline{\beta}_{cb}$ is 0.20 for a d_{med} of 19.4 microns (spray condition A) compared with a $\overline{\beta}_{cb}$ of 0.12 for a d_{med} of 11.5 microns (spray condition C).

Limits of impingement s_{max}. - The rearmost dye trace on a blotter-covered surface is defined as s_{max}. For inlet velocity ratios less than 1.0, decreasing the maximum droplet diameter d_{max} results in progressively smaller outer-cowl s_{max} as shown in figure 5. Inner-cowl s_{max} is reduced with reduced d_{max} for V_i/V_0 greater than 1.0. For example, at a V_i/V_0 of 1.781 (fig. 5(e)), $s_{ic,max}$ is about 0.9 inch compared with 0.2 inch for d_{max} of 63 and 24 microns (spray conditions A and C), respectively. The following four limits of impingement could not be determined accurately because of the asymptotic nature of the $\overline{\beta}$ curves near $\overline{\beta}$ values of zero: (1) $s_{ic,max}$ values for inlet velocity ratios less than 1.0; (2) $s_{oc,max}$ values for V_i/V_0 greater than 1.0; (3) $s_{ic,max}$ and $s_{oc,max}$ for V_i/V_0 of 1.017; and (4) $s_{cb,max}$ values at all inlet velocity ratios. Consequently, values of these impingement limits quoted in subsequent discussions are estimated; however, based on the data available herein and on previous studies with airfoils and bodies of revolution, the general trend of decreasing s_{max} with decreasing d_{max} is preserved.

Effect of angle of attack. - Local impingement efficiencies $\overline{\beta}$ as a function of s for the inlet model at an angle of attack of 4.2° are presented in figure 6 for four inlet velocity ratios, 0.404 to 1.771.

For comparable inlet velocity ratios, the impingement data with inlet angle of attack of 4.2° (fig. 6) differ from that with the inlet at zero angle of attack (fig. 5) as follows: Except for the value of $\overline{\beta}_{max}$ (which is difficult to determine accurately), local impingement efficiency on the cowl inner surface $\overline{\beta}_{ic}$ at an angle of attack at 4.2° (fig. 6) is higher on the leeward than on the windward cowl for $V_i/V_0 < 1.0$. For the outer surface of the cowl and $V_i/V_0 > 1.0$, $\overline{\beta}_{oc}$ is higher on the windward than on the leeward cowl. An arithmetic average of the leeward and windward cowl values of $\overline{\beta}_c$ generally falls close to the value of $\overline{\beta}_c$ at zero angle of attack. As was the case for zero angle of attack, cowl impingement efficiencies greater than 10 percent fall within a few inches of the cowl leading edge. At an angle of attack of 4.2°, values of $\overline{\beta}_{c,max}$ are similar to those at 0°.

The centerbody $\bar{\beta}$ values ($\bar{\beta}_{cb}$) shown in figure 6 increase with increasing inlet velocity ratio with the windward values always higher than the leeward; again, an arithmetic average of the two falls close to $\bar{\beta}_{cb}$ at zero angle of attack. Evidence of a concentration zone appears in the $\bar{\beta}_{cb}$ data near an s_{cb} of 20 inches (see figs. 6(c) and (d)) similar to that previously discussed for zero angle of attack.

Although no impingement data were taken on a 12 o'clock position (plane that is perpendicular to α-plane), results from previous studies on bodies of revolution at small angles of attack (ref. 23) indicate that an arithmetic average of windward and leeward data should give an adequate estimation.

For all inlet velocity ratios studied, impingement limits on the inner surface of the windward cowl are generally less at an angle of attack of 4.2° than at zero angle of attack. Impingement limits on the outer surface of the leeward cowl are less at 4.2° than at zero angle of attack. Similarly, impingement limits on the outer and inner surfaces of the windward and leeward cowl, respectively, are generally larger at 4.2° than at zero angle of attack. For the angles of attack studied, the greatest changes in impingement limit occur on the inner surface of the windward cowl for $V_i/V_0 < 1.0$. For example, at spray condition A and a V_i/V_0 of about 0.67, $s_{ic,max}$ is $25\frac{1}{2}$ inches at zero angle of attack (fig. 5(b)) compared with a windward cowl $s_{ic,max}$ of 8 inches at an angle of attack of 4.2° (fig. 6(b)). Compared with the 0° data, $s_{ic,max}$ trends for an angle of attack of 4.2° and $V_i/V_0 < 1.0$ are the result of the windward cowl being in effect at lower angle of attack relative to the approaching droplets as previously discussed. Similar reasoning accounts for the other $s_{c,max}$ trends shown in figure 6.

Within the accuracy of determining limits of impingement, centerbody s_{max} values ($s_{cb,max}$) are not significantly different at an angle of attack of 4.2° than at 0°. As might be expected, the effect of small angle of attack on $s_{cb,max}$ is damped out as airflow proceeds farther into the inlet.

Total Concentration Factor

As defined herein (as in ref. 1), the total concentration factor $\bar{C}_t$ is the ratio of water ingested by the inlet plane A_i (nacelle station 1.9) to the water contained in a free-stream tube of the A_i cross section. A plot of $\bar{C}_t$ as a function of inlet velocity ratio is presented in figure 7 for zero angle of attack and the three spray conditions.

Inlet air streamlines are indicated schematically at the top of figure 7 for A_0/A_i less than, equal to, or greater than 1.0. As previously discussed, infinitely small droplets have trajectories coincident with the air streamlines. Therefore, the water passing through the inlet plane A_i (water ingested) is the same as that passing through an A_0 plane (free-stream cross-sectional area of inlet air stream tube), or for infinitely small droplets and incompressible flow:

$$C_t = \left(\frac{\text{Water through } A_i}{\text{Water through } A_0}\right)\left(\frac{A_0}{A_i}\right) = \frac{A_0}{A_i} = \frac{V_i}{V_0}$$

(For a cloud with uniform droplet size, total concentration factor is C_t.) This condition is indicated by a dotted line at 45° in figure 7. For infinitely large droplets (straight-line trajectories), the water passing through the inlet plane A_i is the same as that passing through a free-stream annulus of the A_i cross section; therefore, C_t is 1.0. This condition is indicated by the horizontal dotted line in figure 7. At a V_i/V_0 of 1.0, air streamlines and droplet trajectories are essentially parallel, and $\overline{C}_t$ equals 1.0 for all droplet diameters.

Data on figure 7 fall within the limiting boundaries just described. At $V_i/V_0 < 1.0$, some of the droplets contained within a free-stream annulus of the A_i cross section cross the inlet air streamlines and enter the inlet, while others diverge enough to pass outside the inlet; thus, $V_i/V_0 < \overline{C}_t < 1.0$. As droplet diameter increases, increasingly more droplets cross the inlet air streamlines. For example, at a V_i/V_0 of 0.39, $\overline{C}_t$ is 0.55 and 0.40 for a d_{med} of 19.4 and 11.5 microns, respectively. At $V_i/V_0 > 1.0$, all the droplets contained within a free-stream annulus of the A_i cross section enter the inlet. In addition, some of the droplets contained between a free-stream annulus of the A_i cross section and the inlet air streamlines enter the inlet while the remainder cross the inlet air streamlines and pass outside the inlet; thus, $1.0 < \overline{C}_t < V_i/V_0$. As droplet diameter increases and $V_i/V_0 > 1.0$, increasingly more droplets cross the converging inlet air streamlines, and $\overline{C}_t$ is reduced. For example, at a V_i/V_0 of 1.6, $\overline{C}_t$ is 1.38 and 1.25 for a d_{med} of 11.5 and 19.4 microns, respectively.

Theoretical data on total concentration factor for some particular annular inlet configurations at inlet velocity ratios of 0.7 and 1.0 are available in reference 1. If a configuration is selected from reference 1 as nearly like the model studied herein as possible, the theoretically calculated values of $\overline{C}_t$ are in good agreement with the experimental as indicated by the tailed symbols on figure 7. A comparison of configurations is presented schematically in figure 8.

Although the value of $\overline{C}_t$ for fully annular inlets of this type appears relatively insensitive to changes in the inlet configuration as indicated by figures 7 and 8, local impingement rates or limits of impingement on the inlet surfaces, or both, probably will be significantly different for small changes in the inlet configuration.

Generalization of Impingement and Ingestion Characteristics

4704

In the literature, local and total collection efficiencies and impingement limit are usually presented as functions of K and φ. The parameter K indicates the inertia of the droplet, and φ represents the deviation of the droplet drag forces from Stokes' law. As discussed and illustrated in references 26 and 22, s_{max}, $\overline{\beta}$, and $\overline{E}_m$ can be correlated with reasonable accuracy with one independent parameter - the modified inertia parameter; likewise, the amount of water ingested should be amenable to this treatment. The modified inertia parameter K_0 ($K_0 = \lambda/\lambda_s K$; $\lambda/\lambda_s = f(Re_0)$, see ref. 22) accounts for the pertinent impingement variables of droplet size, body size, airspeed, and altitude. Use of the K_0 parameter yields a set of points for any dependent impingement factor (s_{max}, $\overline{\beta}$, or $\overline{E}_m$) that can be essentially represented by a single curve, independent of φ; this curve is approximately the solution using Stokes' law for sphere (droplet) drag. From experience with the K_0 parameter, limited experimental or theoretical impingement and ingestion data can be reasonably extended or interpolated over a wide range of variables although no complete substantiation of its significance or validity is currently available.

With a cloud composed of nonuniform droplet sizes, impingement and ingestion efficiencies are correlated with $K_{0,med}$ (K_0 calculated with d_{med}). Because the limit of impingement is a function of the maximum droplet diameter present in the cloud, s_{max} will be correlated with $K_{0,max}$ (K_0 calculated with d_{max}).

Local impingement efficiency $\overline{\beta}$. - Cowl and centerbody $\overline{\beta}$ as a function of $K_{0,med}$ is presented for the inlet studied at zero angle of attack and V_i/V_0 values from 0.387 to 1.781 in figure 9. Local impingement efficiency $\overline{\beta}$ is a function of surface distance as well as V_i/V_0 and $K_{0,med}$. Therefore, for illustrative purposes, the s-distances of figure 9 were selected arbitrarily from the basic data plots (fig. 5). Values of $\overline{\beta}_{c,max}$ are dotted in figure 9(a), and values of $\overline{\beta}_{cb,max}$ are not plotted in figure 9(b) because of the difficulty in accurately establishing their absolute values as discussed previously.

For a particular s_c (fig. 9(a)), increasing $K_{0,med}$ (increasing droplet size) results in increasing $\overline{\beta}_c$ for all inlet velocity ratios. At fixed values of $K_{0,med}$ and s_c, $\overline{\beta}_{ic}$ decreases and $\overline{\beta}_{oc}$ increases with an increase in inlet velocity ratio. As previously discussed, cowl impingement is concentrated very near the leading edge over a wide range of inlet velocity ratios.

For the centerbody in figure 9(b), $\overline{\beta}_{cb}$ at a particular s_{cb} increases with increasing $K_{0,med}$ for all values of V_i/V_0. For s_{cb} greater than 1/2 inch, $\overline{\beta}_{cb}$ values are less than 0.3 for the entire range of variables studied. Although $s_{cb,max}$ is between 24 and 27 inches for all conditions investigated, $\overline{\beta}_{cb}$ values are generally less than 0.1 for s_{cb} greater than 8 inches.

Total impingement efficiency $\overline{E}_m$. - As defined herein, $\overline{E}_m$ is a surfacewise integration of $\overline{\beta}$ divided by a constant reference area A_i (eq. (C2)). Therefore, as expected, the values of $\overline{E}_m$ for the inner cowl, outer cowl, and centerbody as a function of $K_{0,med}$, which are plotted in figure 10, follow the same general trends as previously discussed for $\overline{\beta}$. The definition of $\overline{E}_m$ and the presentation of inner- and outer-cowl data separately are for convenience in determining inlet ingestion values, as discussed subsequently. At a particular value of $K_{0,med}$, inner-cowl $\overline{E}_m$ (fig. 10(a)) decreases with increasing values of V_i/V_0; concurrently, outer-cowl $\overline{E}_m$ increases. Total cowl (inner plus outer) $\overline{E}_m$ values are a minimum at V_i/V_0 nearest 1.0, varying from 0.035 to 0.06 as $K_{0,med}$ varies from 0.0186 to 0.0439, respectively. Total cowl $\overline{E}_m$ values are a maximum at the two extremes of inlet velocity ratios studied; $\overline{E}_m$ at both conditions increases from about 0.06 to about 0.15 as $K_{0,med}$ increases from 0.0186 to 0.0439, respectively.

Centerbody $\overline{E}_m$ values (fig. 10(c)) over the range of $K_{0,med}$ and V_i/V_0 studied fall into a relatively narrow band generally less than a value of 0.05. The combined $\overline{E}_m$ value of cowl and centerbody is a maximum at a V_i/V_0 of 1.781 and varies from 0.088 to 0.233 as $K_{0,med}$ varies from 0.0186 to 0.0439, respectively.

Limits of impingement s_{max}. - The estimated values of cowl and centerbody s_{max} as a function of $K_{0,max}$ are presented for the inlet at zero angle of attack in figures 11(a) and (b), respectively. At a particular value of inlet velocity ratio, $s_{c,max}$ values increase with increasing $K_{0,max}$. In general, varying inlet velocity ratio has a marked effect on $s_{c,max}$, analogous to the effect of varying angle of attack of an airfoil as previously discussed. Centerbody $s_{cb,max}$ is essentially independent of inlet velocity ratio for the range of conditions studied.

#10#

Unimpinged water ingested. - Part of the water ingested by the inlet plane (nacelle station 1.9) impinges on the inner-cowl and centerbody surfaces; and the remainder, except for the impingement on the three centerbody support struts which was not measured, does not impinge but passes freely through the annular duct to the compressor face (nacelle station 85). Although nacelle station 36 (see fig. 2) was the downstream limit of blotter coverage used herein, the lack of impingement this far aft for the entire range of conditions studied and the geometry of the internal ducting between nacelle stations 36 and 85 indicate that the measured impingement values comprise all the significant internal impingement upstream of nacelle station 85. Thus, the unimpinged water ingested is determined herein by subtracting the inner cowl plus centerbody (less forebody, see sketch (c), appendix C) impingement upstream of nacelle station 36 from the water ingested by the inlet plane. This unimpinged water (ingested by nacelle station 36) is presented in dimensionless terms as a function of $K_{0,med}$ and V_i/V_0 in figure 12. The unimpinged water increases with increasing inlet velocity ratio. For values of $V_i/V_0 < 1.0$, the unimpinged water increases with $K_{0,med}$; the reverse is true for $V_i/V_0 > 1.0$. In the latter case, increasingly more water passes outside the inlet as $K_{0,med}$ (or d_{med}) increases, as previously discussed.

By assuming the water passing through nacelle station 36 (fig. 12) is uniformly mixed and by knowing the inlet airflow areas and velocities (fig. 2(b)), the local average liquid-water content within the inlet and aft of station 36 can be readily calculated. Figure 13 presents the results of such a calculation for nacelle station 85 (simulated compressor face) of the inlet studied at zero angle of attack. In general, for the inlet and range of conditions studied, the results of figure 13 indicate that the local average liquid-water content at the compressor face is not greater than the free-stream value and may be as much as 40 percent less than free stream for inlet velocity ratios near 1.8. Thus, even at inlet velocity ratios less than 1.0, where some droplets not originally in the free-stream tube cross the inlet air streamlines and enter the inlet, the impingement on the internal components of this inlet configuration is sufficient to compensate for the increased water ingestion. By neglecting the unlikely case of unfrozen water running on the inner-cowl and centerbody surfaces as far back as the engine inlet guide vanes, for example, the data of figure 13 indicate that guide-vane icing protection systems designed on the basis of free-stream liquid-water content should be adequate at zero angle of attack for the type of inlet and range of conditions studied.

Total concentration factor $\bar{C}_t$. - Total concentration factor for any condition within the range of $K_{0,med}$ studied is obtained by adding centerbody and inner-cowl impingement efficiency (fig. 10) and the ratio of the unimpinged to available water (fig. 12). For example, consider a V_i/V_0 of 0.667 and a $K_{0,med}$ of 0.0344. Then, from figure 12, the total water passing through nacelle station 36 is 0.68 times that passing through a free-stream area of A_i cross section. Likewise, from figures 10(a) and (c), inner-cowl and centerbody $\bar{E}_m$ values (total impingement to total water available in free-stream tube of A_i cross section, see appendix C) are 0.06 and 0.02, respectively. The summation results in a $\bar{C}_t$ value of 0.76, the same value as previously presented in figure 7. Because $K_{0,med}$ and V_i/V_0 can be varied, a $\bar{C}_t$ plot such as figure 7 may be drawn for any prescribed conditions for the inlet studied at zero angle of attack.

Although not presented explicitly herein, the inlet impingement and ingestion data for an angle of attack of 4.2° may be generalized in the same manner as illustrated and discussed with figures 9 to 13 for zero angle of attack. Total concentration factor as a function of inlet velocity ratio for the inlet at an angle of attack of 4.2° is nearly identical to figure 7 for zero angle of attack.

Concluding Remarks

Reference 24 implies that the unknown impingement of a body may be approximately equal to the known impingement of a reference body provided the local surface pressure (or velocity) distributions of the reference body can be made approximately equal to those of the unknown body by varying angle of attack or chord length or both. In particular, the pressure distributions and surface contours need be similar in the impingement regions of both bodies. Extending this reasoning to an annular inlet such as the type studied herein suggests the possibility of estimating cowl and centerbody impingement from the known impingement of several airfoils (refs. 11 to 18 and 22) and bodies of revolution (refs. 7, 8, 23, and 27). Demonstration or proof of the validity of such an analysis is beyond the scope of this report.

Most of the reported data on droplet size and liquid-water content of natural icing clouds has been obtained with the rotating multicylinder method (ref. 2). Such values are readily converted to the slightly different ones quoted herein for the tunnel cloud (by Joukowski-aspirator method) by figure 19 of reference 22. A sample calculation applying tunnel impingement data to flight conditions is given in reference 22.

SUMMARY OF RESULTS

A full-scale supersonic nose inlet with conical centerbody was studied for cloud droplet impingement and ingestion characteristics at angles of attack of 0° and 4.2° over a range of ratios of inlet to free-stream velocity from about 0.4 to 1.8. The free-stream velocity in the tunnel was constant at Mach 0.237. The results of these studies may be summarized as follows:

1. Impingement and ingestion are functions of the ratio of inlet to free-stream velocity as well as of droplet size. Because experimental and theoretical impingement data for airfoils and bodies of revolution can be reasonably correlated by use of a modified inertia parameter, a similar correlation is suggested for inlet impingement and ingestion characteristics. The modified inertia parameter accounts for flight speed, droplet size, body size, altitude, and temperature.

2. For a particular droplet size and surface location on an inlet component, local impingement efficiencies increase on the outer cowl and centerbody as inlet velocity ratio increases; concurrently, inner-cowl values decrease. Total impingement efficiencies on each of the cowl surfaces and centerbody vary in a like manner. The ratio of water ingested by the inlet plane to that available in a free-stream tube of cross section equal to that at the inlet plane also increases with increasing inlet velocity ratio.

3. Theoretically calculated values of concentration factor or water scooping ratio are in good agreement with experiment for annular inlet configurations.

4. For the inlet and range of conditions studied, converting the unimpinged water ingested through the inlet plane to a uniformly mixed local liquid-water content at the compressor-face plane results in water content values not greater than free-stream values and as much as 40 percent less for inlet velocity ratios near 1.8.

Lewis Flight Propulsion Laboratory
National Advisory Committee for Aeronautics
Cleveland, Ohio, February 19, 1958

4704

CQ-3

APPENDIX A

SYMBOLS

A	area, sq ft
$\overline{C}_t$	total concentration factor or scooping ratio in cloud of tunnel droplet size distribution, defined in eq. (C8), dimensionless
D	diameter of inlet at nacelle station 1.9 (see fig. 2), 2.483 ft
d	droplet diameter, microns (3.28×10^{-6} ft)
$\overline{E}_m$	total impingement efficiency in cloud of tunnel droplet size distribution, defined in eq. (C2), dimensionless
K	droplet inertia parameter, $1.70\times10^{-12}\ d^2V_0/\mu D$ (density of water, 1.94 slugs/cu ft, included in constant), dimensionless
K_0	modified inertia parameter, $(\lambda/\lambda_s)K$, dimensionless
M	Mach number
m	mass-flow rate
m_i/m_0	mass-flow ratio, $\rho_i V_i A_i/\rho_0 V_0 A_i = A_0/A_i = \dfrac{4.337\ M_{85}}{(1+0.2\ M_{85}^2)^3}\dfrac{P_{85}}{P_0}$, herein
P	total pressure
p	static pressure
Re_0	free-stream Reynolds number with respect to droplet, $\dfrac{4.81\times10^{-6} d\rho V_0}{\mu} = \sqrt{K\varphi}$, dimensionless
r	local body radius, in. (see fig. 2)
s	surface distance downstream of reference, in. (see fig. 2)
V	velocity, mph
$\overline{W}_m$	total water impingement rate in cloud of tunnel droplet size distribution, lb/hr
$\overline{W}_\beta$	local water impingement rate in cloud of tunnel droplet size distribution, lb/(hr)(sq ft)

w_t	total liquid-water content of cloud, g/cu m
α	inlet angle of attack, deg
$\overline{\beta}$	local impingement efficiency in cloud of tunnel droplet size distribution, defined in eq. (C1), dimensionless
γ	ratio of specific heats for air, 1.4, dimensionless
λ	true range of droplet as a projectile injected into still air, ft
λ_s	range of droplet as a projectile following Stokes' law, ft
μ	viscosity of air, slugs/(ft)(sec)
ρ	density of air, slugs/cu ft
φ	independent impingement parameter, $\varphi \equiv \dfrac{13.6\,\rho^2 D V_0}{\mu}$, dimensionless

4704

CQ-3 back

Subscripts:

c	cowl surface	See fig. 2
cb	centerbody surface	
i	inlet plane, nacelle station 1.9	
ic	inner-cowl surface	
l	local surface	
max	maximum	
med	volume median	
oc	outer-cowl surface, see fig. 2	
s	surface	
x	cross-sectional to airflow	
0	free stream	
85	nacelle station 85 (simulated compressor face, fig. 2)	

Superscripts:

$\overline{}$ weighted value resulting from effects of tunnel droplet size distribution ($\approx$ Langmuir "D", refs. 22 and 25)

$*$ based on frontal area of saber

APPENDIX B

LOCAL SURFACE VELOCITY DISTRIBUTION ON NOSE-INLET MODEL

From the compressible form of Bernoulli's equation, the ratio of the local surface to the free-stream velocity can be written as

$$\left(\frac{V_l}{V_0}\right)^2 = \frac{\left[1 - \left(\frac{p_l}{P_0}\right)^{\frac{\gamma-1}{\gamma}}\right]\left[2 + (\gamma - 1)M_0^2\right]}{(\gamma - 1)M_0^2}$$

With the tunnel conditions for the dye impingement studies of $M_0 = 0.237$ and $\gamma = 1.4$, then

$$\frac{V_l}{V_0} = 9.49 \sqrt{1 - \left(\frac{p_l}{P_0}\right)^{0.286}} \qquad \text{(B1)}$$

The ratio of local surface to free-stream velocity (from eq. (B1)) as a function of nacelle station and inlet velocity ratio is presented for the inlet studied at angles of attack of 0° and 4.2° in figure 14. These data are uncorrected for tunnel effects.

With the inlet at zero angle of attack (fig. 14(a)), velocity distributions on the inner- and outer-cowl walls forward of nacelle station 10 and at inlet velocity ratios less than 1.0 are similar to those on the lower and upper surfaces, respectively, of an airfoil at angle of attack, as described in the section GENERAL CONSIDERATIONS OF INLET AIRFLOW AND IMPINGEMENT. Centerbody surface velocities increase with increasing inlet velocity ratio, with local values reaching a peak near nacelle station 20 (see fig. 3(a)) then decreasing to the values obtained on the inner cowl.

With the inlet at an angle of attack of 4.2° and an inlet velocity ratio of 1.771 (fig. 14(b)), there is evidence of flow separation on the inner surface of the windward cowl. A similar flow-separated profile occurs on the upper surface of a thin airfoil at an angle of attack of 8° in reference 28. Centerbody surface velocities indicate negligible peripheral variation with the model at an angle of attack of 4.2°.

APPENDIX C

ANALYSIS OF DATA

Colorimetry

Rectangular segments (1/16 by 1 in. near leading edge and 1/8 by $1\frac{1}{2}$ in. in aft region) are punched from the nearly two-dimensional cowl blotters. Circular punches (3/8-in. diameter) are taken from the three-dimensional conical centerbody blotters. The 1/8-inch-wide saber ribbons are trimmed to a uniform length of 1 inch. The dye is dissolved out of each segment with a known quantity of distilled water. The concentration of this solution is determined by the amount of light of a suitable wavelength transmitted through the solution in a calibrated colorimeter. If the original concentration of dye in water solution used in the spray is known, the amount of dye collected on the segment is converted into the weight of water (dye-water solution) that impinged on the blotter segment during the measured exposure time. In this way, the local water impingement rate $\overline{W}_\beta$ is obtained. Details and illustrations of the analysis used herein are given in references 21 and 22.

Impingement Efficiencies

The local rate of water-droplet impingement $\overline{W}_\beta$ and the limit of impingement s_{max} are obtained as a direct result of the dye-tracer technique used herein. The dimensionless impingement parameters $\overline{\beta}$ (local impingement efficiency) and $\overline{E}_m$ (total impingement efficiency) are defined as in references 21 and 25 as

$$\overline{\beta} = \frac{\overline{W}_\beta}{0.329 \, V_0 w_t} \qquad \text{(C1)}$$

$$\overline{E}_m = \frac{1}{A_i} \int_{A_s = 0}^{A_s = A_{s,max}} \overline{\beta} \, dA_s \qquad \text{(C2)}$$

In equation (C2), $A_{s,max}$ is a function of s_{max} and body geometry. The term A_i is generally chosen as the projected frontal area of the body, but any reference area may be selected. For convenience in presenting $\overline{E}_m$ values of inlet cowl and centerbody herein, A_i (cross-sectional area of the airflow annulus at the inlet plane, nacelle station 1.9, 4.576 sq ft) is used as the reference area.

Total Impingement and Ingestion Rates

From equations (C1) and (C2) the total dimensional impingement rate $\overline{W}_m$ in pounds per hour can be generally expressed as

$$\overline{W}_m = \int_{A_s=0}^{A_s=A_{s,max}} \overline{W}_\beta \, dA_s = 0.329 \, V_0 w_t \int_{A_s=0}^{A_s=A_{s,max}} \overline{\beta} \, dA_s = 0.329 \, V_0 w_t \overline{E}_m A_i \tag{C3}$$

Cowl and centerbody. - Because the cross sections of the inlet cowl and centerbody were circular,

$$dA_s = \frac{2\pi}{144} r \, ds, \text{ sq ft}$$

By choosing the leading edge of the inlet lips (nacelle station 1.9) as the dividing line between impingement on the inner and outer cowls, the total cowl impingement can be written as

$$\begin{aligned} \overline{W}_{m,cowl} &= \int_{A_{s,ic}=0}^{A_{s,ic}=A_{s,ic,max}} \left(\overline{W}_\beta \, dA_s\right)_{ic} + \int_{A_{s,oc}=0}^{A_{s,oc}=A_{s,oc,max}} \left(\overline{W}_\beta \, dA_s\right)_{oc} \\ &= 0.329 \, V_0 w_t \frac{2\pi}{144} \left[\int_{s_{ic}=0}^{s_{ic}=s_{ic,max}} \left(\overline{\beta} r \, ds\right)_{ic} + \int_{s_{oc}=0}^{s_{oc}=s_{oc,max}} \left(\overline{\beta} r \, ds\right)_{oc} \right] \end{aligned} \tag{C4}$$

The total centerbody impingement rate can be written as

$$\overline{W}_{m,centerbody} = \int_{A_{s,cb}=0}^{A_{s,cb}=A_{s,cb,max}} \left(\overline{W}_\beta \, dA_s\right)_{cb}$$

or

$$\overline{W}_{m,centerbody} = 0.329 \, V_0 w_t \frac{2\pi}{144} \int_{s_{cb}=0}^{s_{cb}=s_{cb,max}} \left(\overline{\beta} r \, ds\right)_{cb} \tag{C5}$$

Annular flow areas. - The water flow rates through the annular flow areas at nacelle stations 6.7 and 25.5 (see fig. 2) were obtained from the impingement rates of the forward and rear sabers, respectively. These measured impingement rates are less than the water flow rates through each annulus because the total collection efficiency of the sabers, $\overline{E}_m^*$, is less than 100 percent. Saber $\overline{E}_m^*$ values have been determined experimentally and are in the order of 90 percent. The sabers were mounted within a few degrees of a perpendicular to the nacelle axis. Thus the change in annular flow area (in sq ft) at a saber plane can be expressed as

$$dA_x = \frac{2\pi}{144} r\ dr$$

Therefore, from equation (C3) the total water flow rate through an annular flow area is

$$\overline{W}_{m,\text{annulus}} = \int_{A_x = 0}^{A_x = \text{total annular flow area}} \left(\frac{\overline{W}_\beta}{\overline{E}_m^*} dA_x\right)_{\text{saber}}$$

$$= \frac{2\pi}{144\ \overline{E}_m^*} \int_{r = r_{cb}}^{r = r_{ic}} \left(\overline{W}_\beta r\ dr\right)_{\text{saber}} \qquad \text{(C6)}$$

Inlet ingestion. - The water ingested by the inlet is defined as that which is airborne through the inlet plane (nacelle station 1.9).[2] Schematically, the $\overline{W}_m$ (ingested) can be represented as

---

[2] For the range of conditions covered by these studies, the total forebody impingement rate (see sketch (c)) was less than 2 percent of the total water ingested by the inlet. Therefore, forebody impingement is not reported explicitly herein.

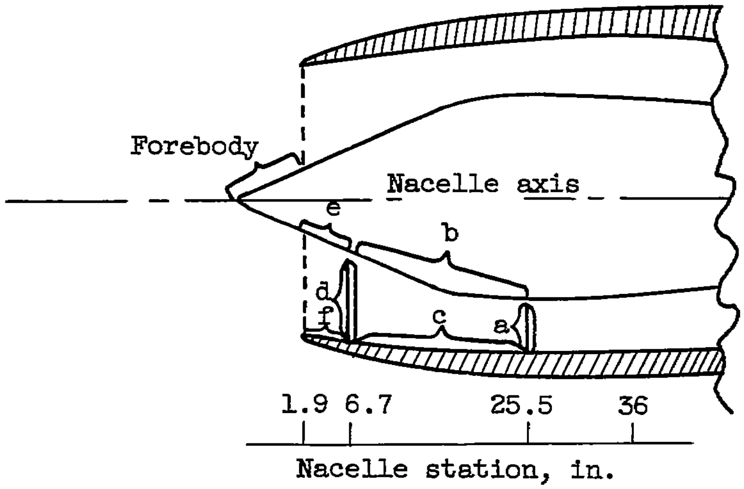

(c)

where the subscripts a to f refer to areas on the sketch and

$$\overline{W}_{m,\text{ingested}} = 1/2\left[(\overline{W}_m)_a + (\overline{W}_m)_b + (\overline{W}_m)_c + (\overline{W}_m)_d\right] + (\overline{W}_m)_e + (\overline{W}_m)_f \tag{C7}$$

The first three terms within brackets of equation (C7) represent the airborne water equivalent to that measured by the forward saber. This equivalent value is averaged with that measured by the forward saber. For all conditions studied, the equivalence is within 10 percent.

Total concentration factor $\overline{C}_t$ (water scooping ratio). - As defined in reference 1 the total concentration factor ((water scooping ratio or ingestion efficiency)/100, percent) is written as

$$\overline{C}_t = \frac{\overline{W}_{m,\text{ingested}}}{\overline{W}_m \text{ (contained in free-stream tube of } A_i \text{ cross section)}}$$

$$= \frac{\overline{W}_{m,\text{ingested}}}{0.329\ V_0 A_i w_t} \tag{C8}$$

REFERENCES

1. Brun, Rinaldo J.: Cloud-Droplet Ingestion in Engine Inlet with Inlet Velocity Ratios of 1.0 and 0.7. NACA TN 3593, 1956.

2. Brun, R. J., Lewis, W., Perkins, P. J., and Serafini, J. S.: Impingement of Cloud Droplets on a Cylinder and Procedure for Measuring Liquid-Water Content and Droplet Sizes in Supercooled Clouds by Rotating Multicylinder Method. NACA Rep. 1215, 1955. (Supersedes NACA TN's 2903, 2904, and NACA RM E53D23.)

3. Dorsch, Robert G., Saper, Paul G., and Kadow, Charles F.: Impingement of Water Droplets on a Sphere. NACA TN 3587, 1955.

4. Lewis, William, and Brun, Rinaldo J.: Impingement of Water Droplets on a Rectangular Half Body in a Two-Dimensional Incompressible Flow Field. NACA TN 3658, 1956.

5. Hacker, Paul T., Brun, Rinaldo J., and Boyd, Bemrose: Impingement of Droplets in 90° Elbows with Potential Flow. NACA TN 2999, 1953.

6. Hacker, Paul T., Saper, Paul G., and Kadow, Charles F.: Impingement of Droplets in 60° Elbows with Potential Flow. NACA TN 3770, 1956.

7. Dorsch, Robert G., Brun, Rinaldo J., and Gregg, John L.: Impingement of Water Droplets on an Ellipsoid with Fineness Ratio 5 in Axisymmetric Flow. NACA TN 3099, 1954.

8. Brun, Rinaldo J., and Dorsch, Robert G.: Impingement of Water Droplets on an Ellipsoid with Fineness Ratio 10 in Axisymmetric Flow. NACA TN 3147, 1954.

9. Dorsch, Robert G., and Brun, Rinaldo J.: Variation of Local Liquid-Water Concentration About an Ellipsoid of Fineness Ratio 5 Moving in a Droplet Field. NACA TN 3153, 1954.

10. Brun, Rinaldo J., and Dorsch, Robert G.: Variation of Local Liquid-Water Concentration About an Ellipsoid of Fineness Ratio 10 Moving in a Droplet Field. NACA TN 3410, 1955.

11. Brun, Rinaldo J., and Vogt, Dorothea E.: Impingement of Water Droplets on NACA 65A004 Airfoil at 0° Angle of Attack. NACA TN 3586, 1955.

12. Brun, Rinaldo J., Gallagher, Helen M., and Vogt, Dorothea E.: Impingement of Water Droplets on NACA 65A004 Airfoil and Effect of Change in Airfoil Thickness from 12 to 4 Percent at 4° Angle of Attack. NACA TN 3047, 1953.

13. Brun, Rinaldo J., Gallagher, Helen M., and Vogt, Dorothea E.: Impingement of Water Droplets on NACA 65A004 Airfoil at 8° Angle of Attack. NACA TN 3155, 1954.

4704

14. Brun, Rinaldo J., Serafini, John S., and Moshos, George J.: Impingement of Water Droplets on an NACA 65_1-212 Airfoil at an Angle of Attack of 4°. NACA RM E52B12, 1952.

15. Brun, Rinaldo J., Gallagher, Helen M., and Vogt, Dorothea E.: Impingement of Water Droplets on NACA 65_1-208 and 65_1-212 Airfoils at 4° Angle of Attack. NACA TN 2952, 1953.

16. Dorsch, Robert G., and Brun, Rinaldo J.: A Method for Determining Cloud-Droplet Impingement on Swept Wings. NACA TN 2931, 1953.

17. Brun, R. J., and Vogt, Dorothea E.: Impingement of Cloud Droplets on 36.5-Percent-Thick Joukowski Airfoil at Zero Angle of Attack and Discussion of Use as Cloud Measuring Instrument in Dye-Tracer Technique. NACA TN 4035, 1957.

18. Guibert, A. G., Janssen, E., and Robbins, W. M.: Determination of Rate, Area, and Distribution of Impingement of Waterdrops on Various Airfoils from Trajectories Obtained on the Differential Analyzer. NACA RM 9A05, 1949.

19. Serafini, John S.: Impingement of Water Droplets on Wedges and Double-Wedge Airoils at Supersonic Speeds. NACA Rep. 1159, 1954. (Supersedes NACA TN 2971.)

20. Bergrun, Norman R.: An Empirical Method Permitting Rapid Determination of the Area, Rate, and Distribution of Water-Drop Impingement on an Airfoil of Arbitrary Section at Subsonic Speeds. NACA TN 2476, 1951.

21. von Glahn, Uwe H., Gelder, Thomas F., and Smyers, William H., Jr.: A Dye-Tracer Technique for Experimentally Obtaining Impingement Characteristics of Arbitrary Bodies and a Method for Determining Droplet Size Distribution. NACA TN 3338, 1955.

22. Gelder, Thomas F., Smyers, William H., Jr., and von Glahn, Uwe: Experimental Droplet Impingement on Several Two-Dimensional Airfoils with Thickness Ratios of 6 to 16 Percent. NACA TN 3839, 1956.

23. Lewis, James P., and Ruggeri, Robert S.: Experimental Droplet Impingement on Four Bodies of Revolution. NACA TN 4092, 1957.

24. von Glahn, Uwe H.: Use of Truncated Flapped Airfoils for Impingement and Icing Tests of Full-Scale Leading-Edge Sections. NACA RM E56E11, 1956.

4704

CQ-4 back

25. Langmuir, Irving, and Blodgett, Katherine B.: A Mathematical Investigation of Water Droplet Trajectories. Tech. Rep. No. 5418, Air Materiel Command, AAF, Feb. 19, 1946. (Contract No. W-33-038-ac-9151 with General Electric Co.)

26. Sherman, P., Klein, J. S., and Tribus, M.: Determination of Drop Trajectories by Means of an Extension of Stokes' Law. Eng. Res. Inst., Univ. Mich., Apr. 1952. (Air Res. and Dev. Command, USAF, Contract AF 18(600)-51.)

27. Torgeson, W. L., and Abramson, A. E.: A Study of Heat Requirements for Anti-Icing Radome Shapes with Dry and Wet Surfaces. Tech. Rep. 53-284, WADC, Sept. 1953. (Contract AF 33(616)-85, RDO No. 664-802.)

28. Gray, Vernon H.: Correlations Among Ice Measurements, Impingement Rates, Icing Conditions, and Drag Coefficients for Unswept NACA 65A004 Airfoil. NACA TN 4151, 1957.

4704

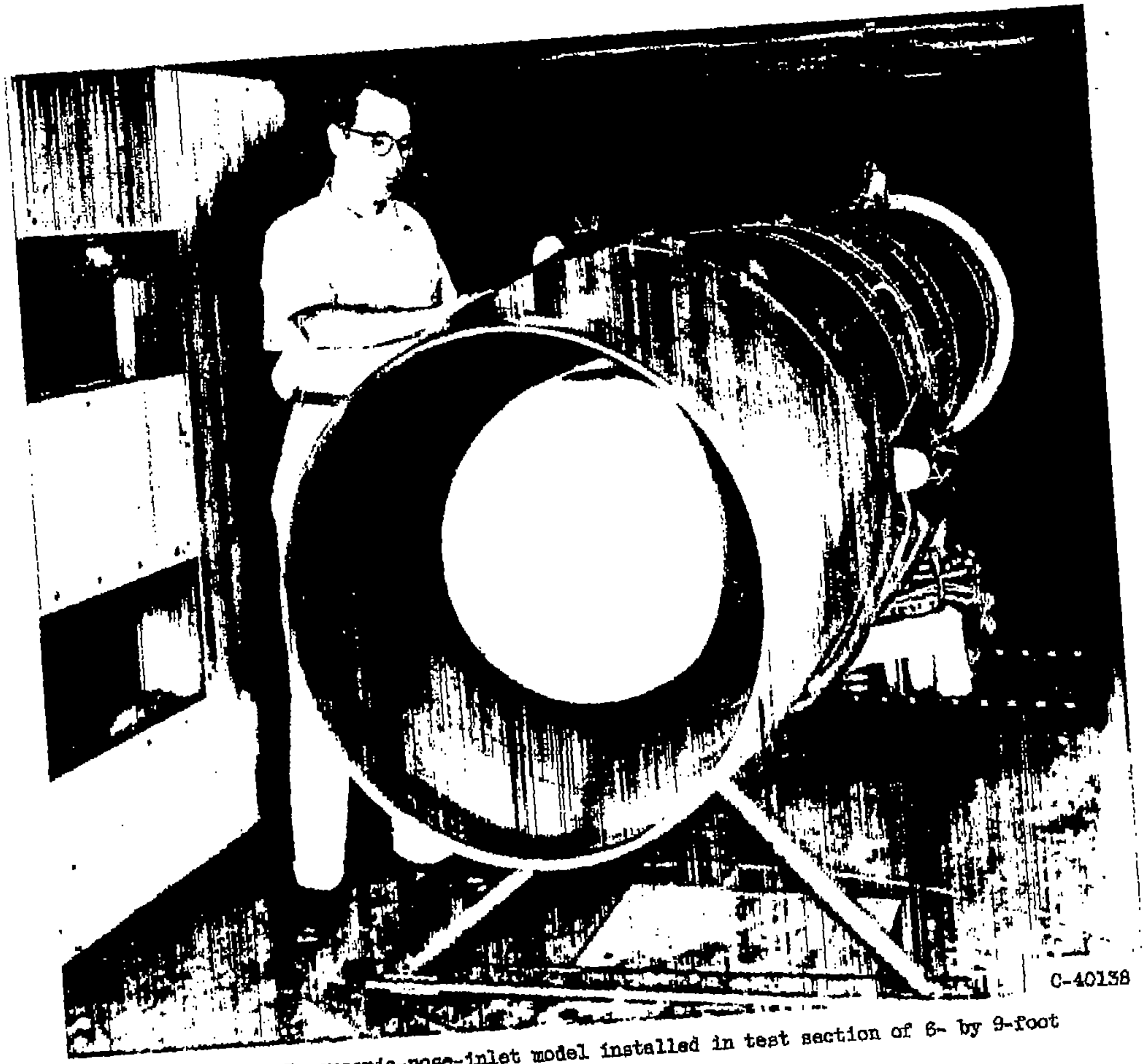

C-40138

Figure 1. - Supersonic-nose-inlet model installed in test section of 6- by 9-foot NACA Lewis icing tunnel.

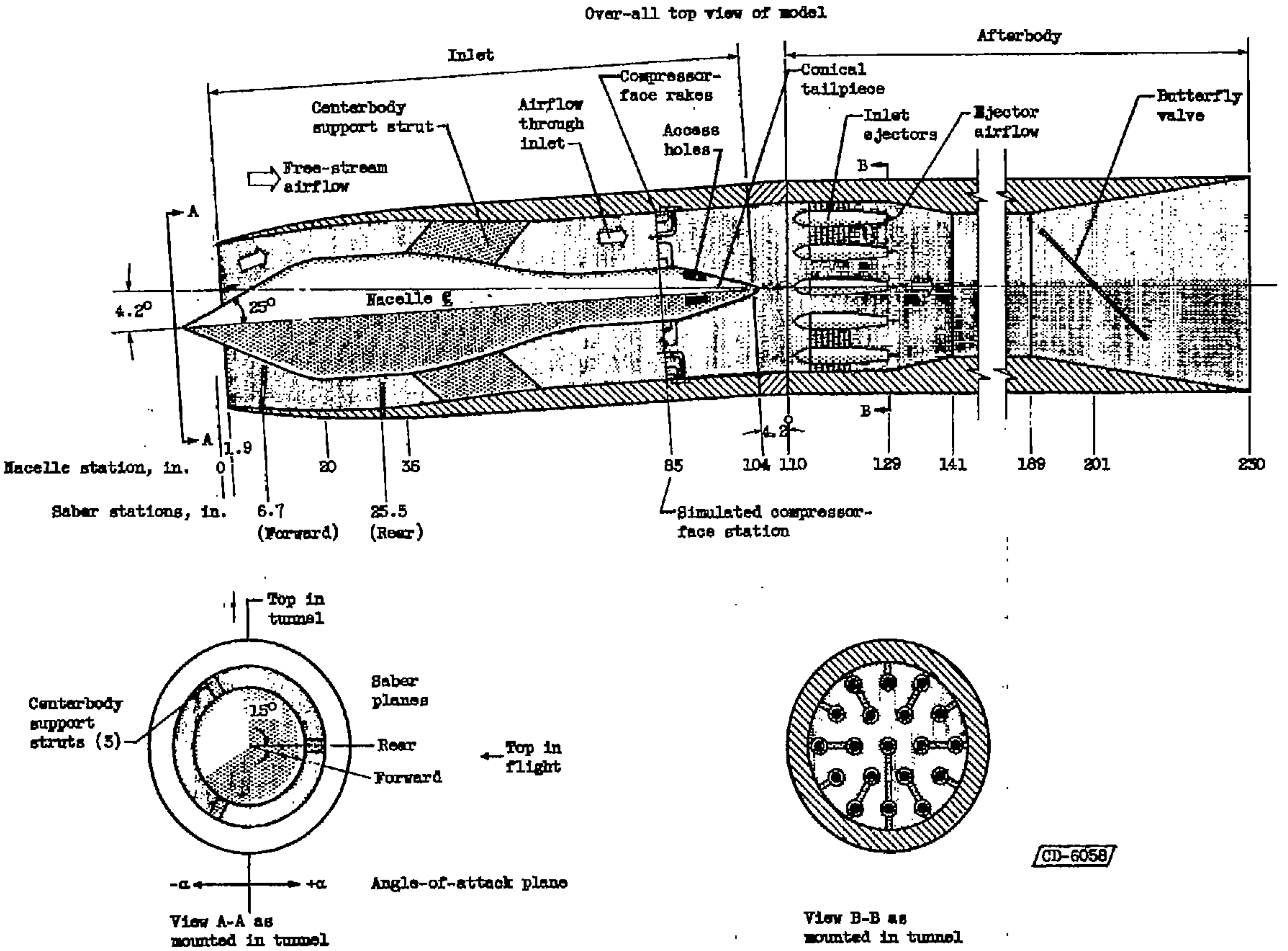

(a) Over-all schematic drawing of inlet and afterbody (inlet at angle of attack of 4.2°).

Figure 2. - Geometry of supersonic-nose-inlet model.

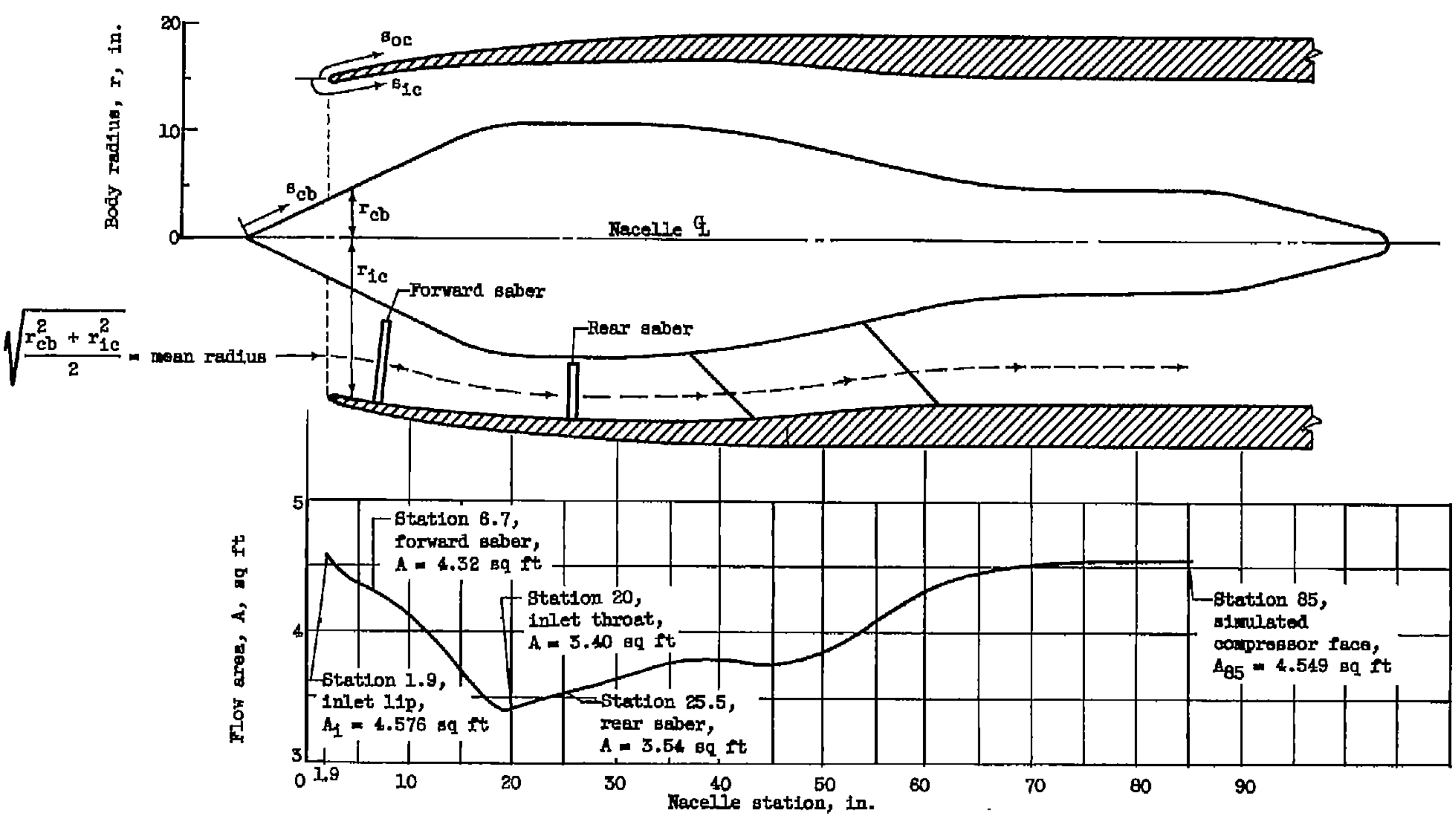

(b) Airflow areas within inlet.

Figure 2. - Continued. Geometry of supersonic-nose-inlet model.

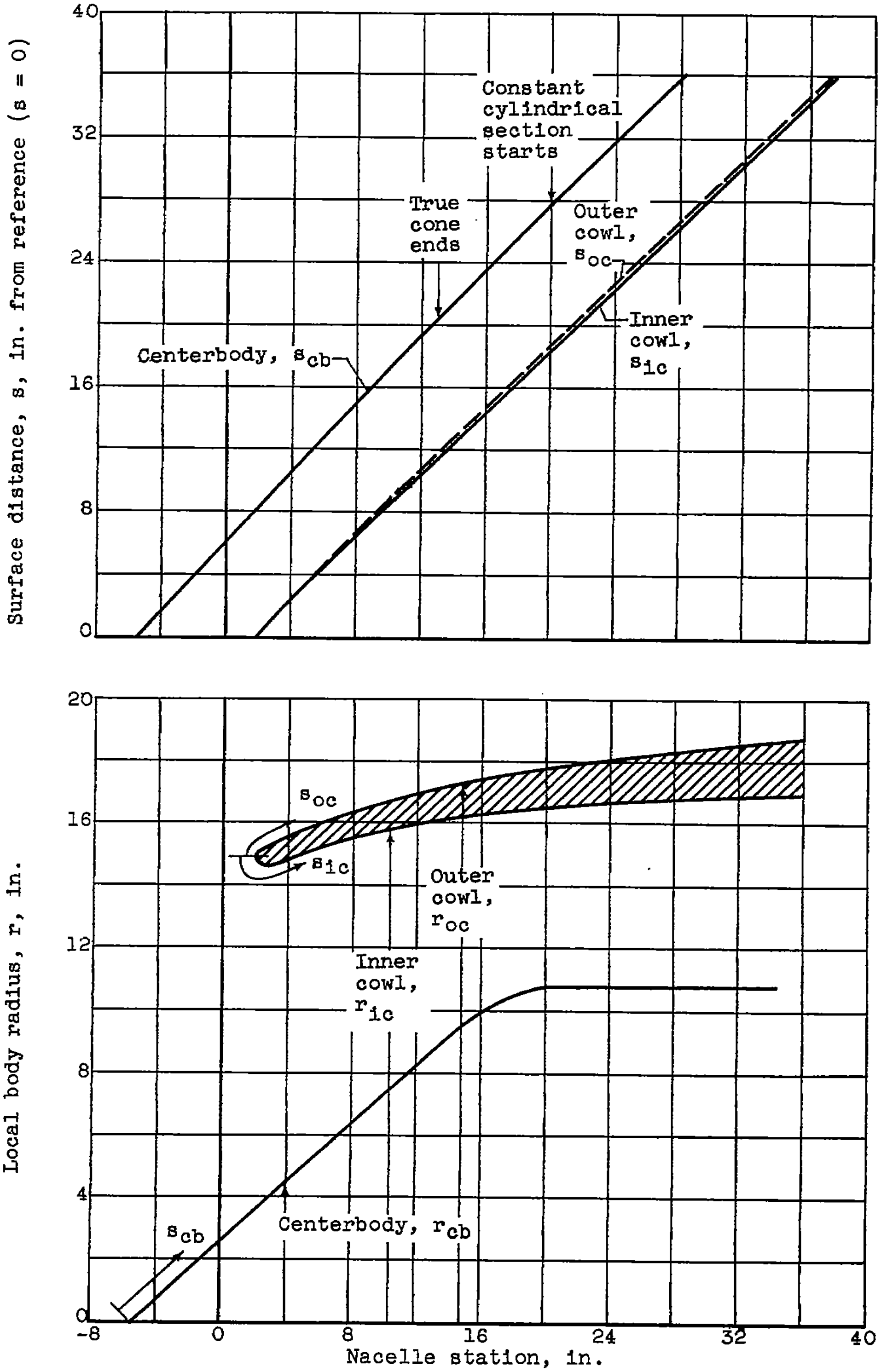

(c) Local body radius and surface distance of inlet components.

Figure 2. - Concluded. Geometry of supersonic-nose-inlet model.

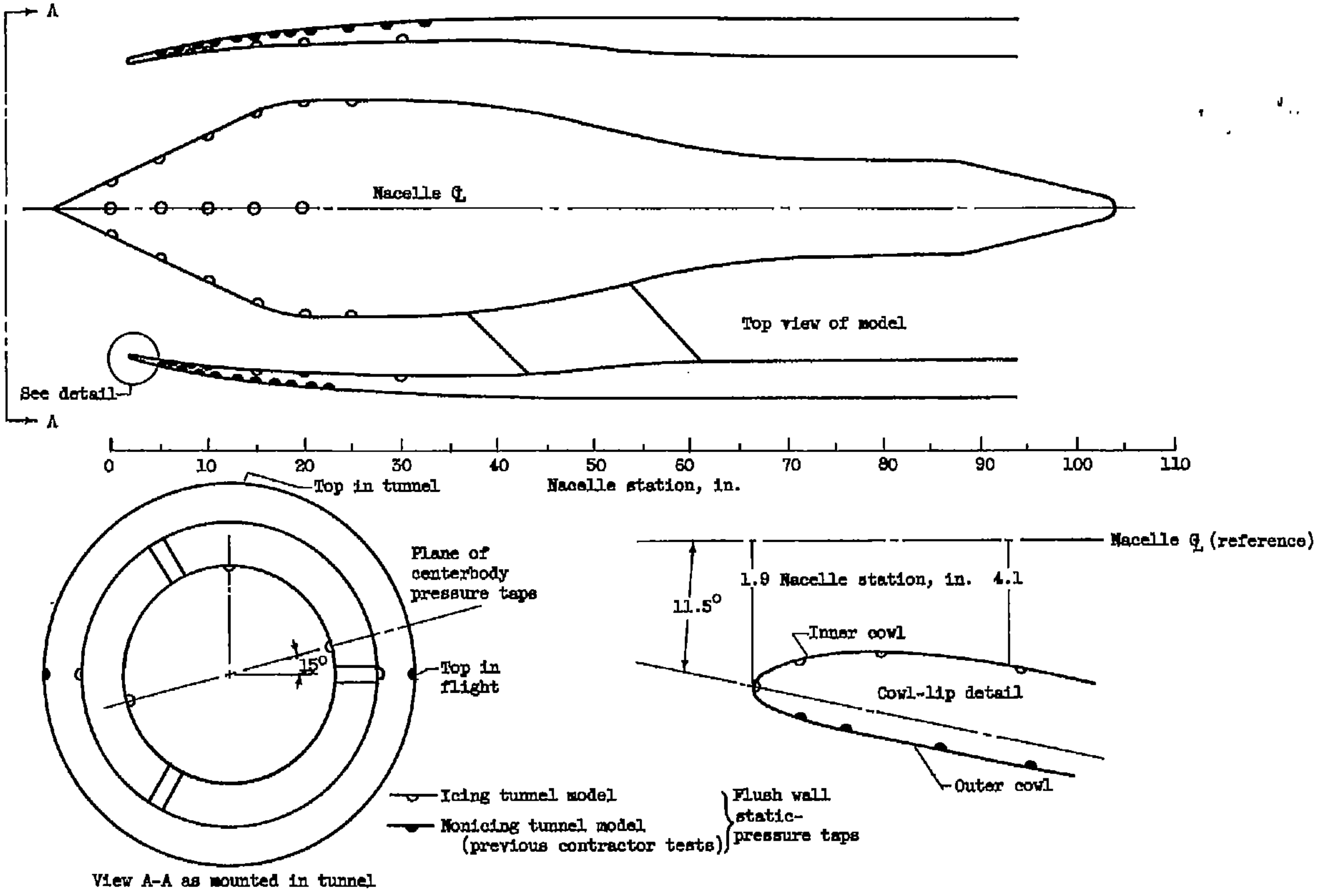

(a) Schematic drawing of cowl and centerbody static-pressure taps.

Figure 3. - Pressure instrumentation of inlet model.

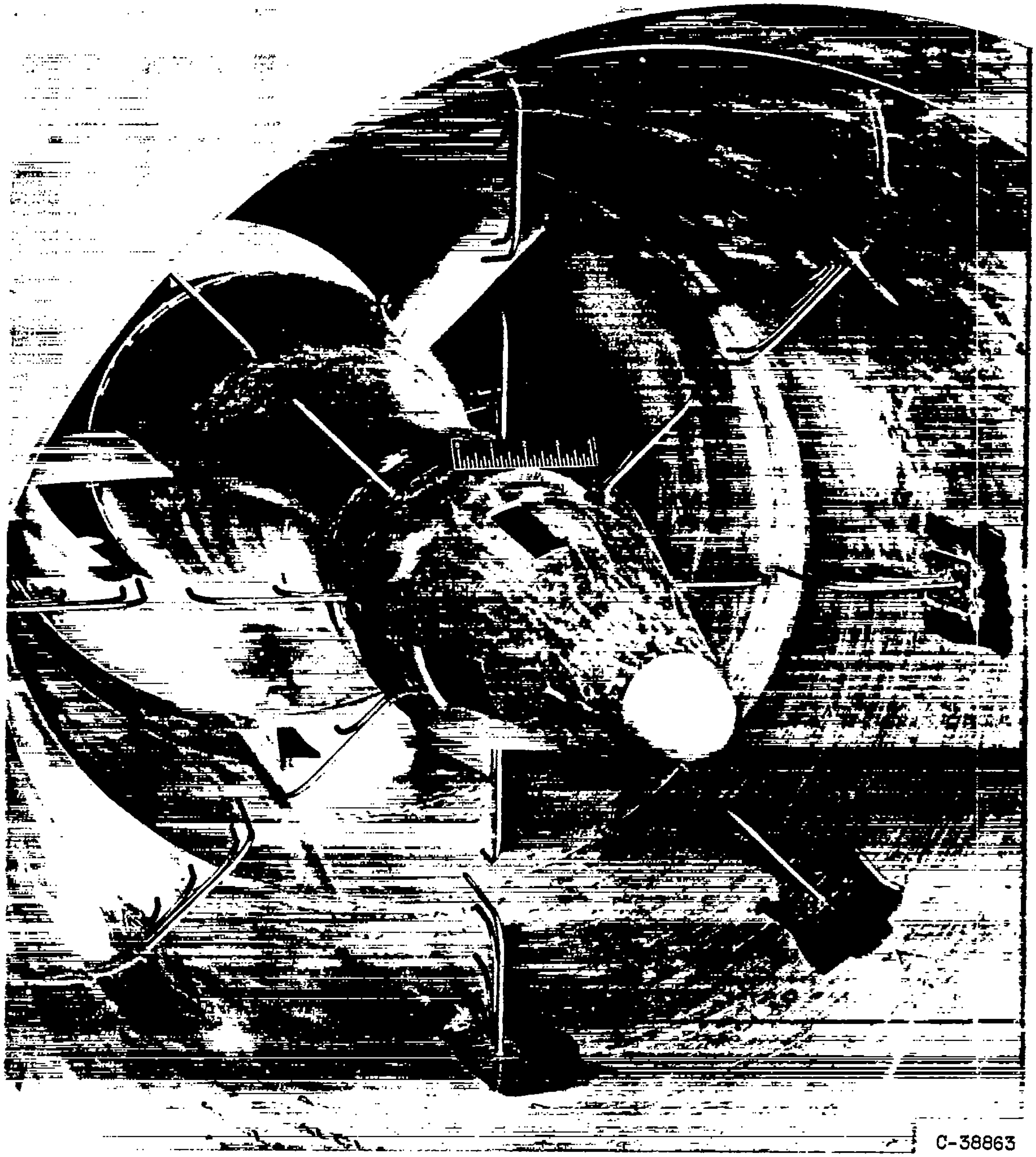

C-38863

(b) Photograph looking upstream at compressor-face rakes.

Figure 3. - Continued. Pressure instrumentation of inlet model.

Instrumentation

● Total-pressure rakes
○ Static-pressure rakes
◓ Flush wall static-pressure taps
— — — Outline of centerbody support struts located approximately 3 ft upstream of compressor-face plane

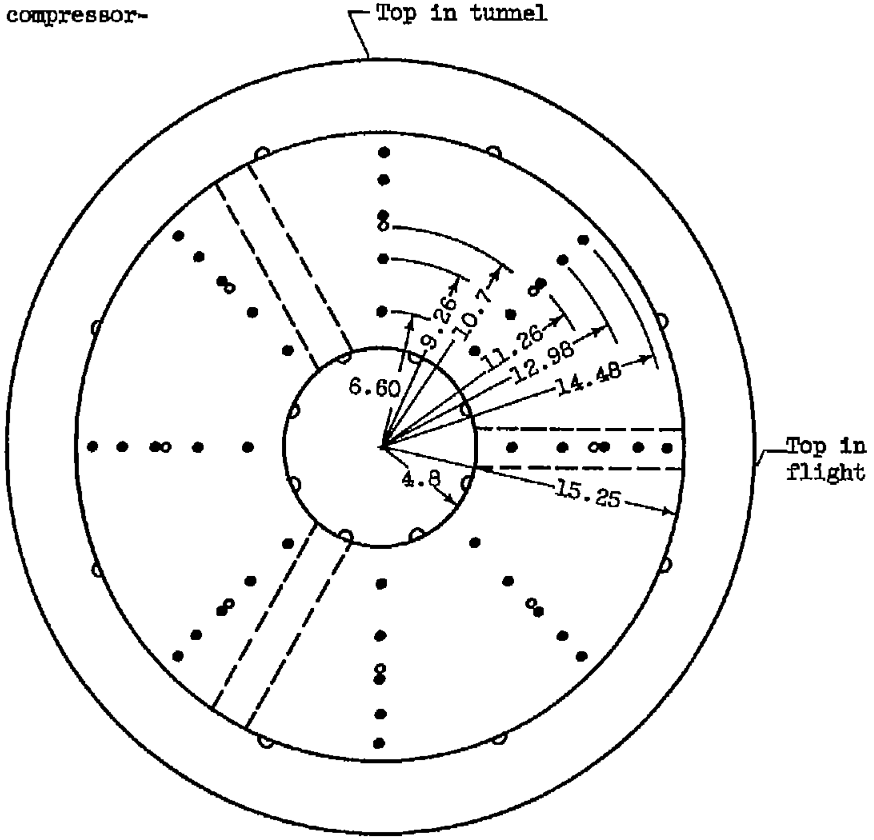

(c) Schematic cross section looking downstream at nacelle station 85 (compressor face) showing location of pressure tubes and taps. (All dimensions in inches.)

Figure 3. - Concluded. Pressure instrumentation of inlet model.

4704

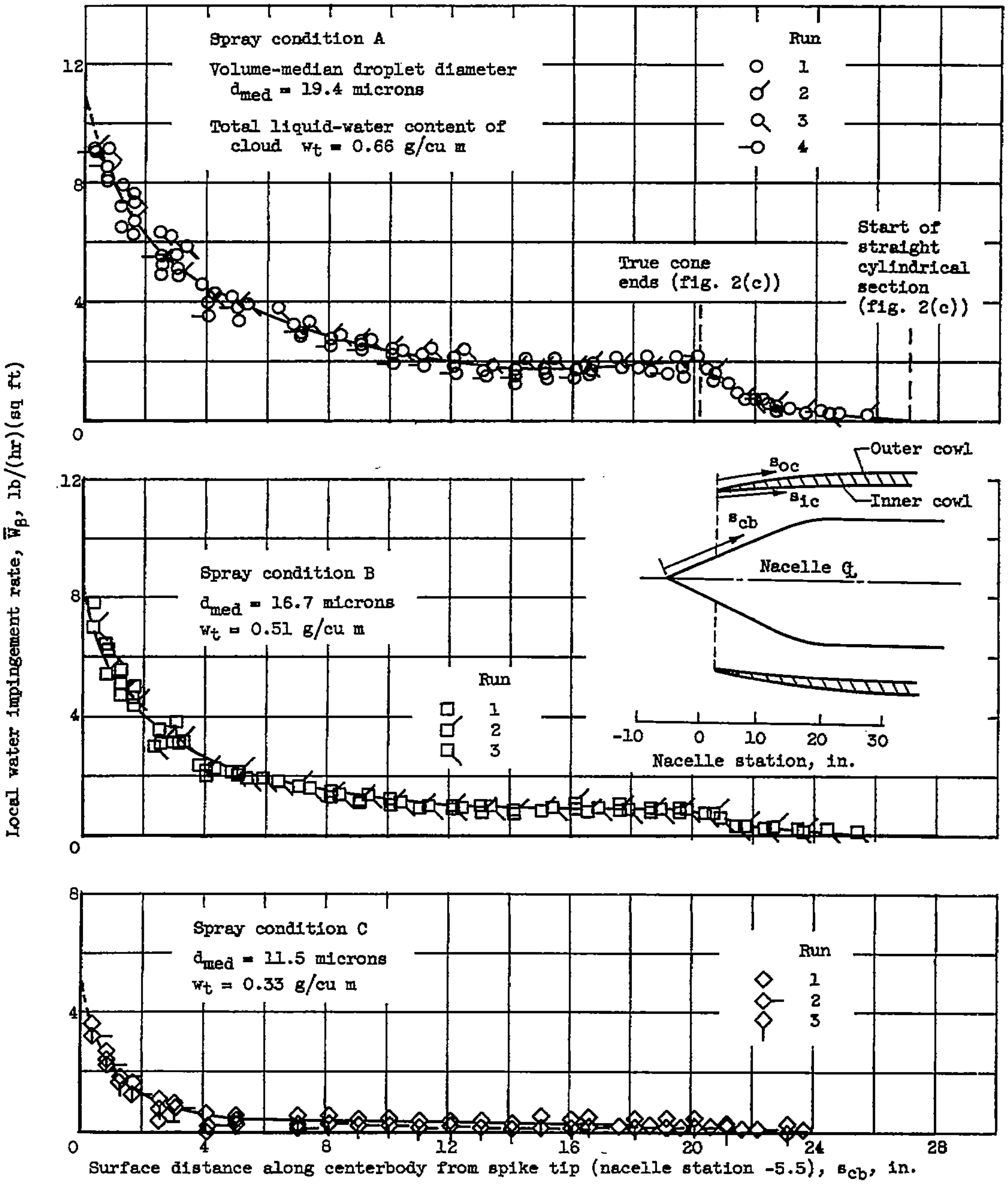

(a) Centerbody impingement.

Figure 4. - Typical water impingement rates on supersonic-nose-inlet model. Angle of attack, 0°; inlet velocity ratio, 1.333.

4704

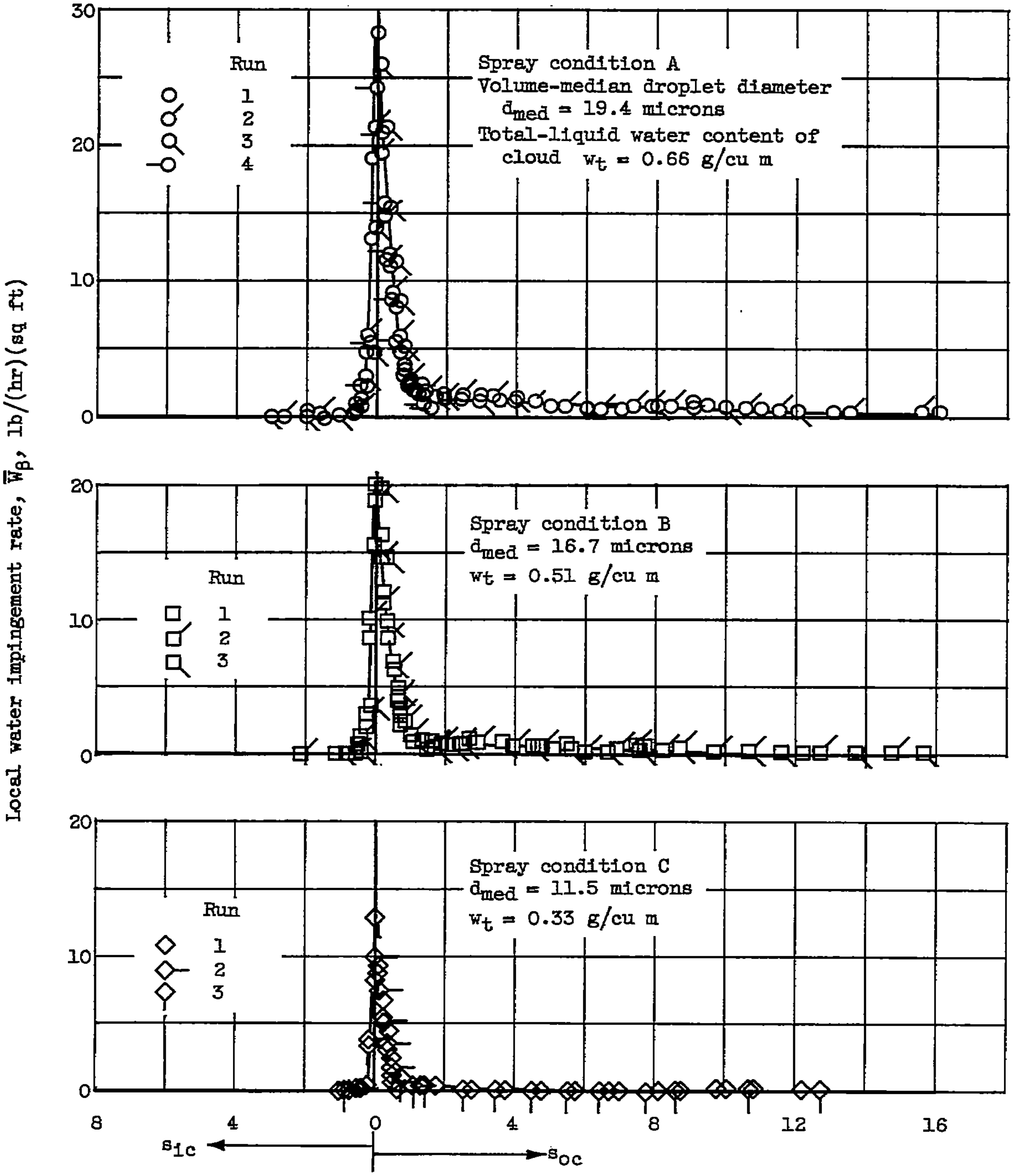

(b) Cowl impingement.

Figure 4. - Concluded. Typical water impingement rates on supersonic-nose-inlet model. Angle of attack, 0°; inlet velocity ratio, 1.333.

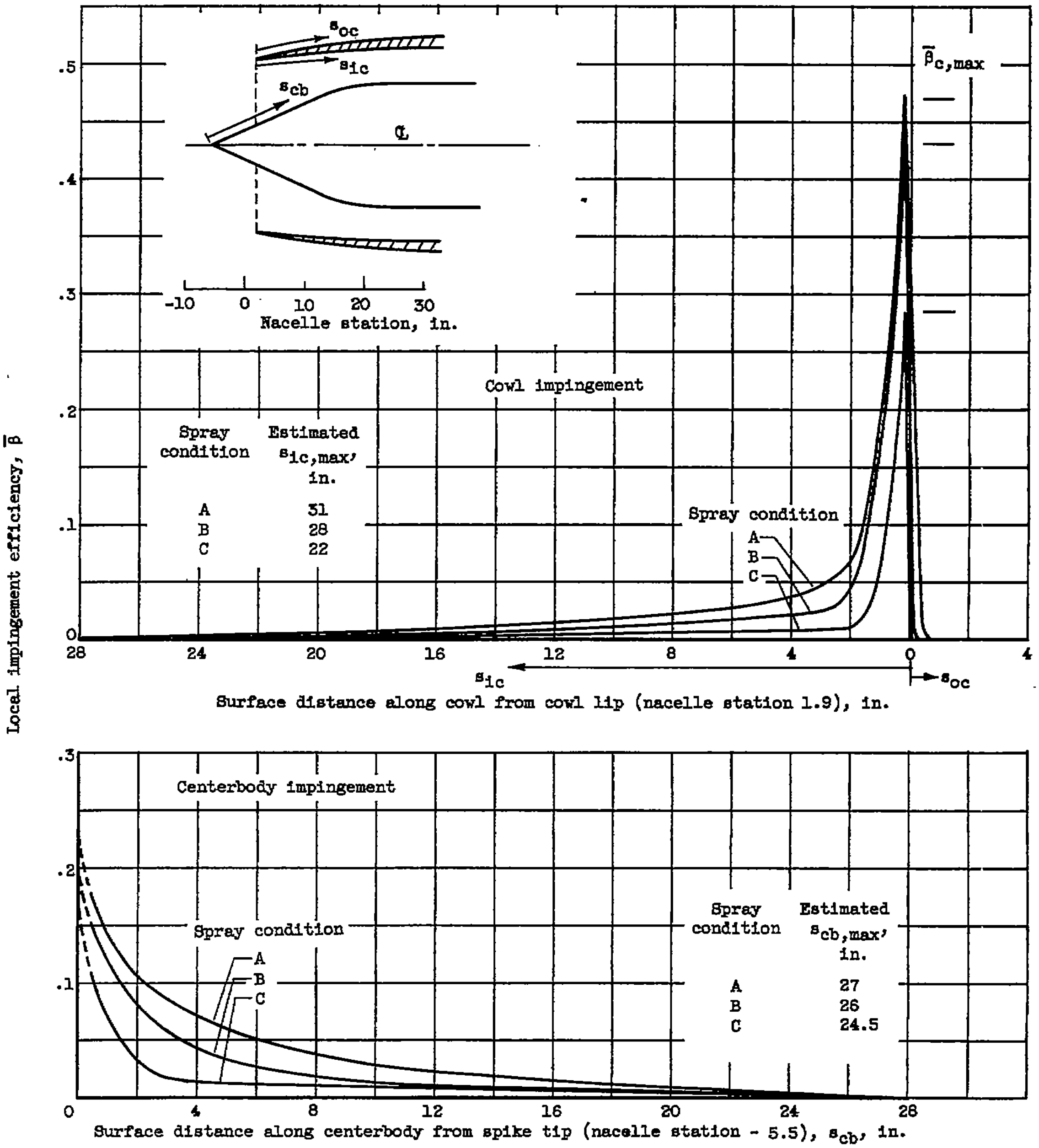

(a) Inlet velocity ratio, 0.387.

Figure 5. - Local impingement efficiency of cowl and centerbody of supersonic-nose-inlet model. Angle of attack, 0°.

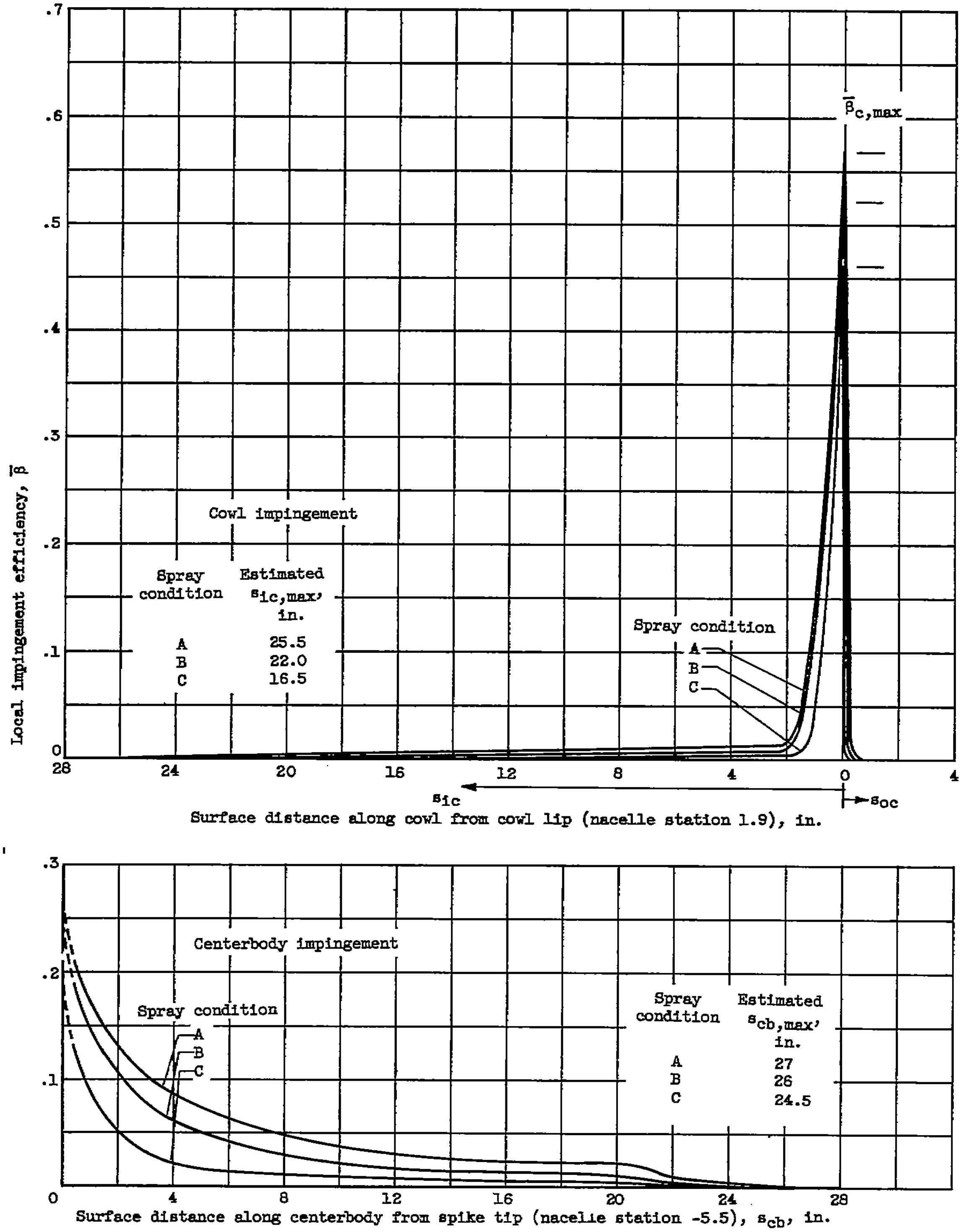

(b) Inlet velocity ratio, 0.667.

Figure 5. - Continued. Local impingement efficiency of cowl and centerbody of supersonic-nose-inlet model. Angle of attack, 0°.

4704

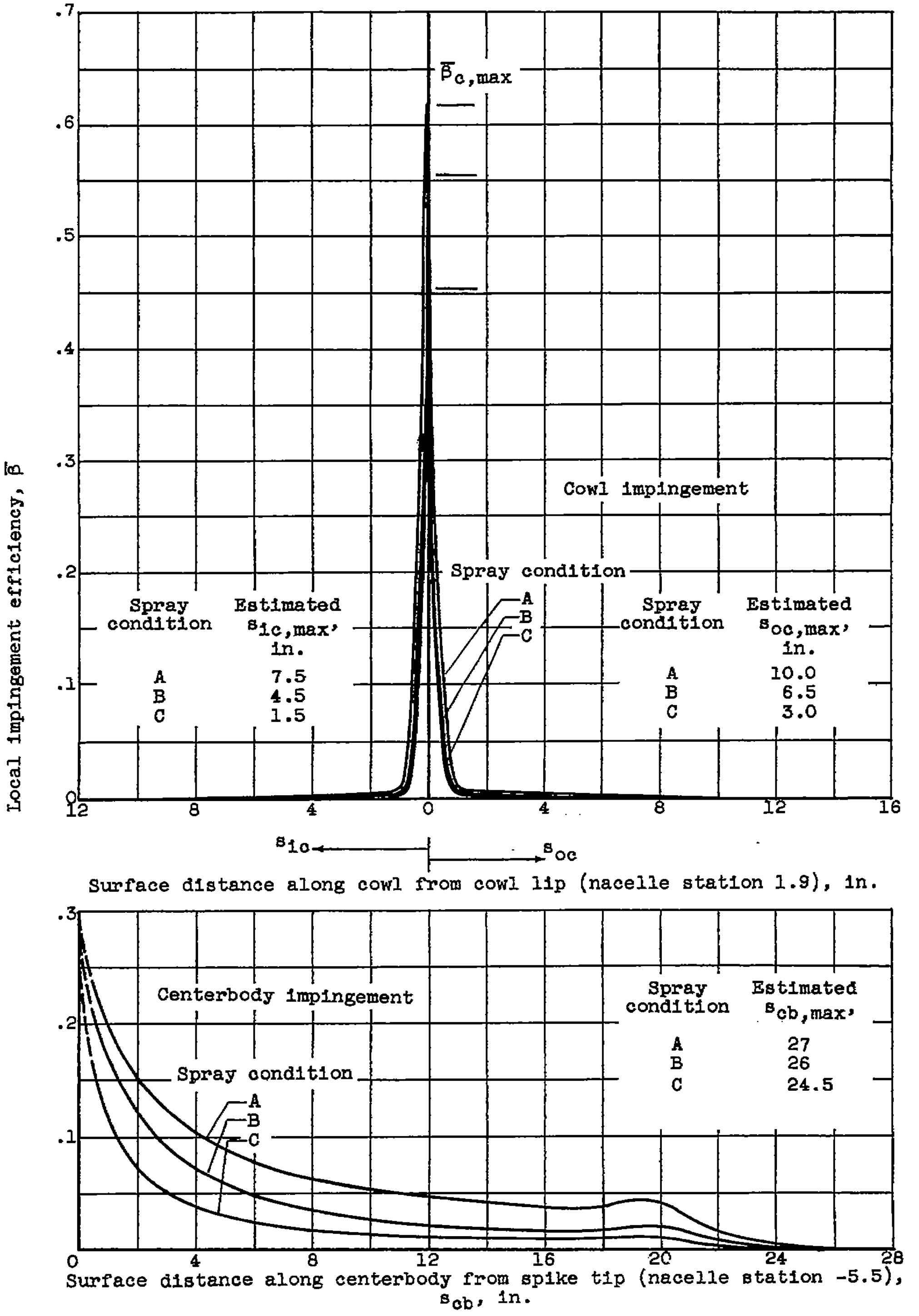

(c) Inlet velocity ratio, 1.017.

Figure 5. - Continued. Local impingement efficiency of cowl and centerbody of supersonic-nose-inlet model. Angle of attack, 0°.

4704

CQ-6

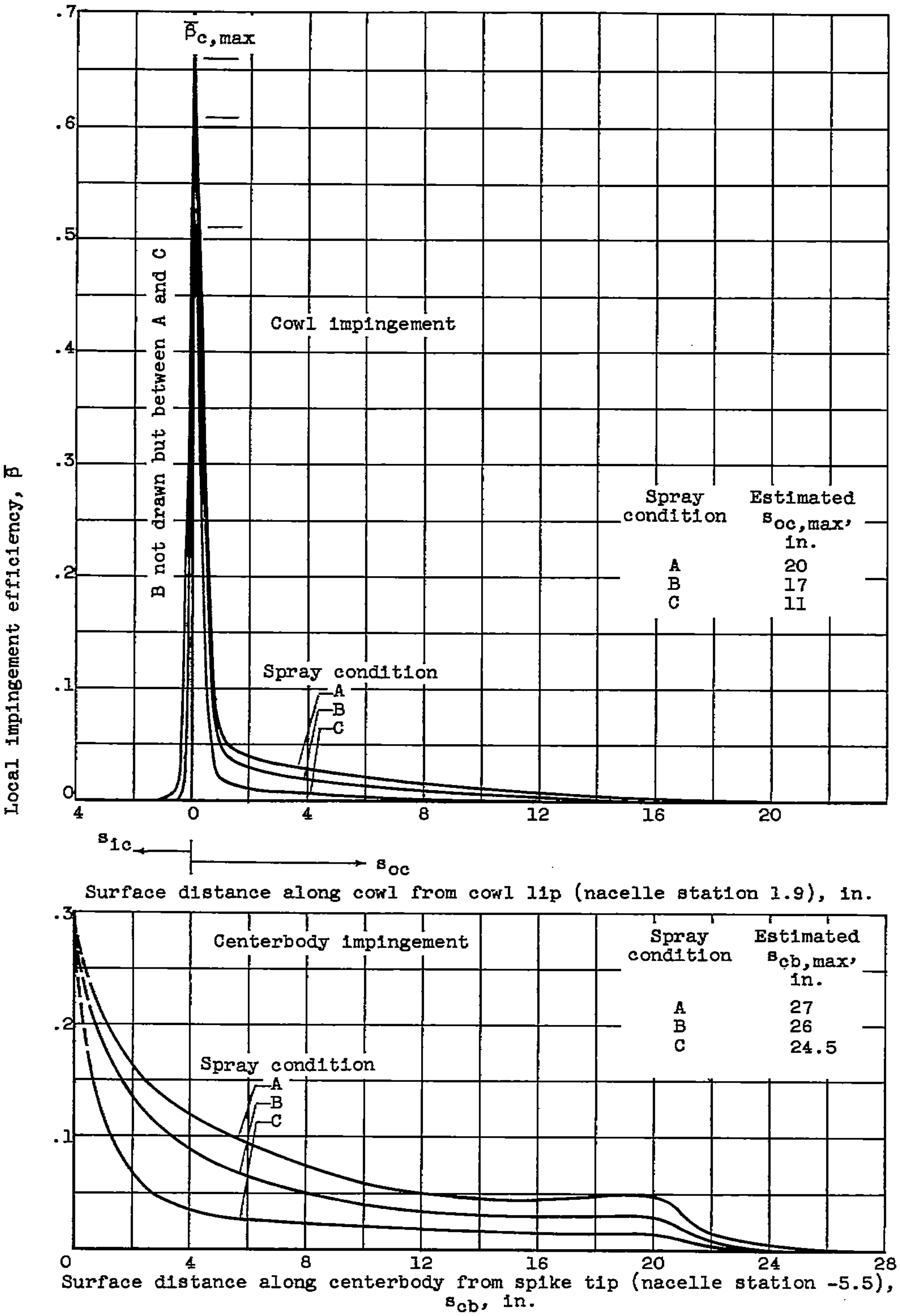

(d) Inlet velocity ratio, 1.333.

Figure 5. - Continued. Local impingement efficiency of cowl and centerbody of supersonic-nose-inlet model. Angle of attack, 0°.

4704

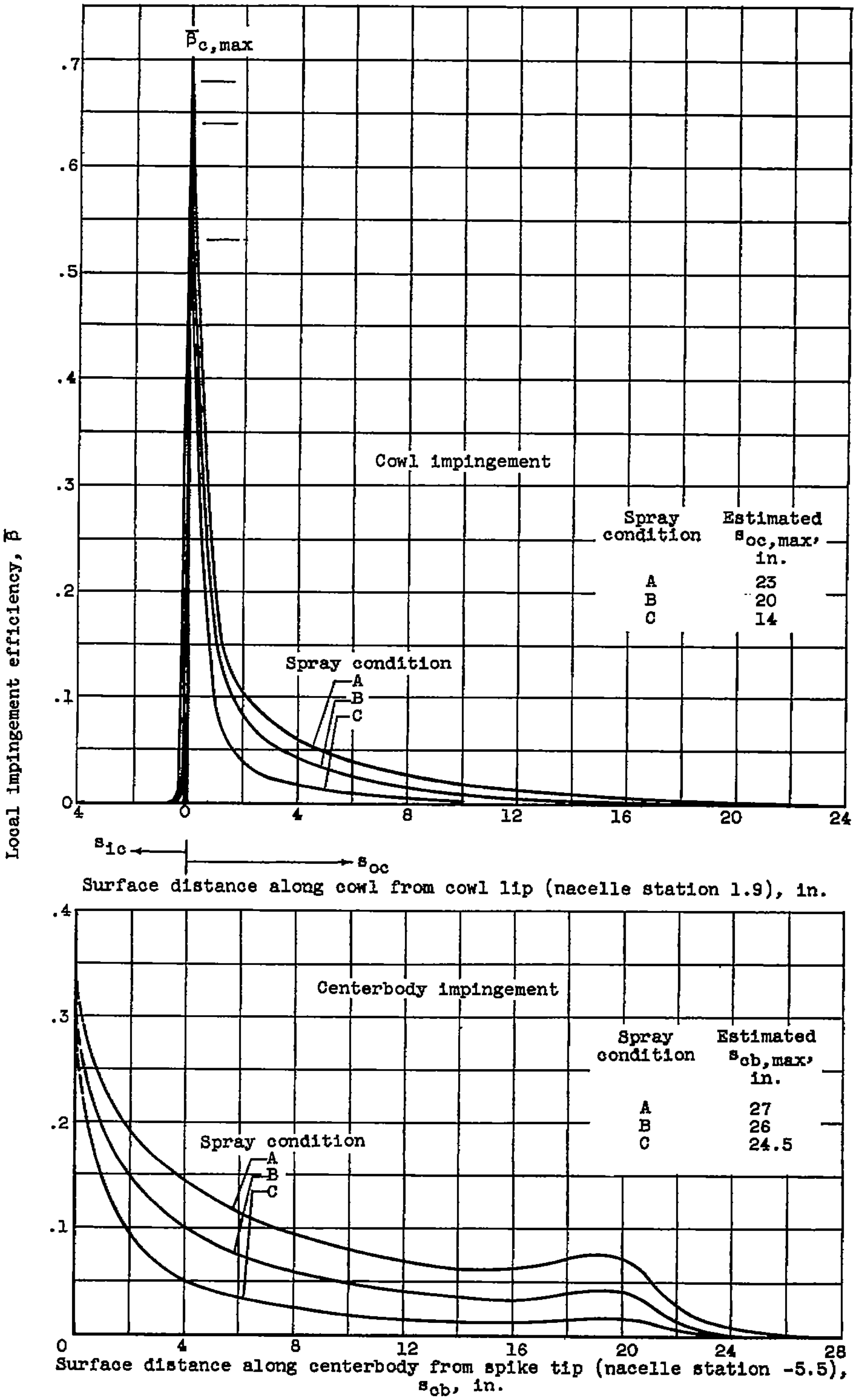

(e) Inlet velocity ratio, 1.781.

Figure 5. - Concluded. Local impingement efficiency of cowl and centerbody of supersonic-nose-inlet model. Angle of attack, 0°.

4704

CQ-6 back

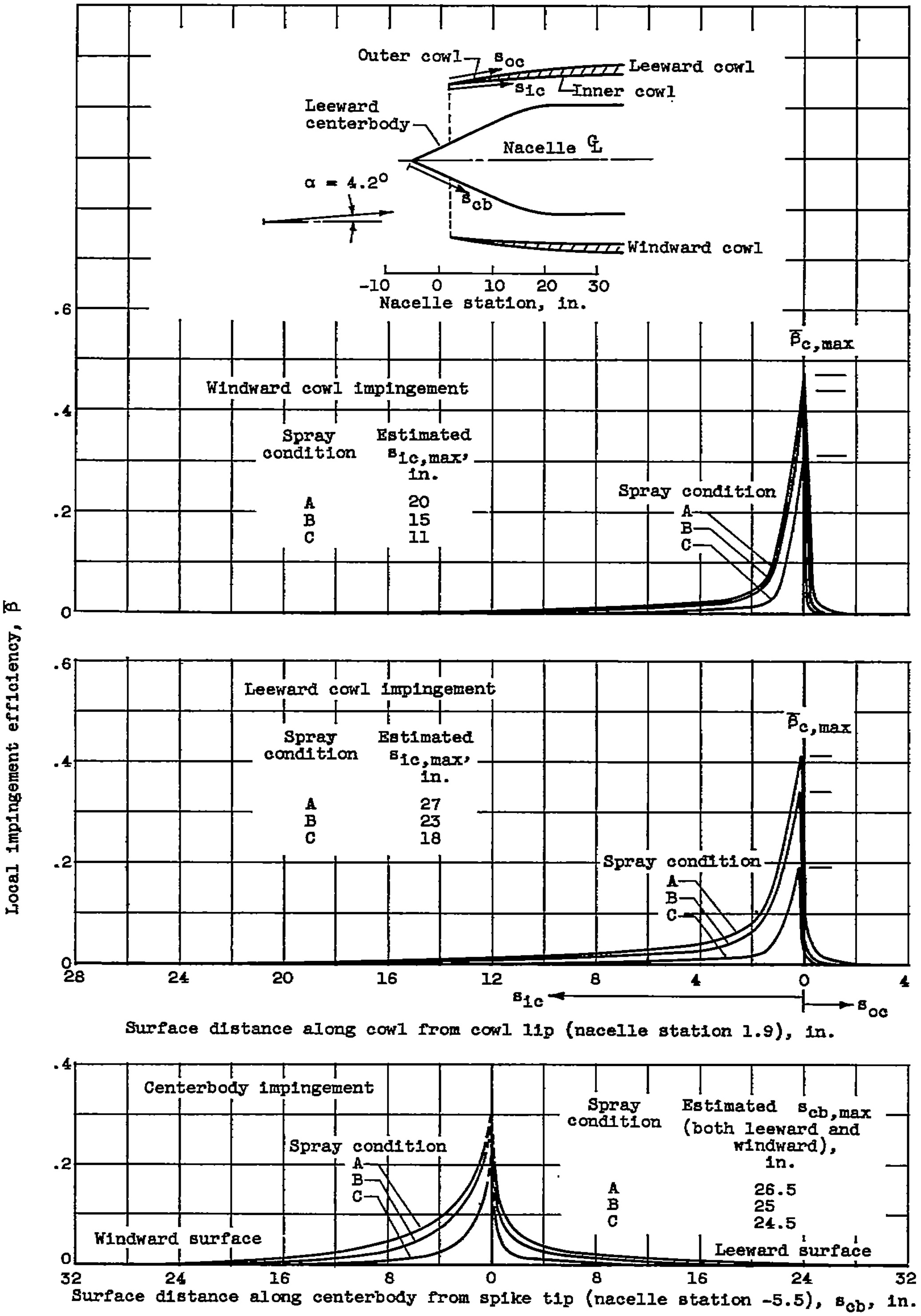

(a) Inlet velocity ratio, 0.404.

Figure 6. - Local impingement efficiency of cowl and centerbody of supersonic-nose-inlet model. Angle of attack, 4.2°.

4704

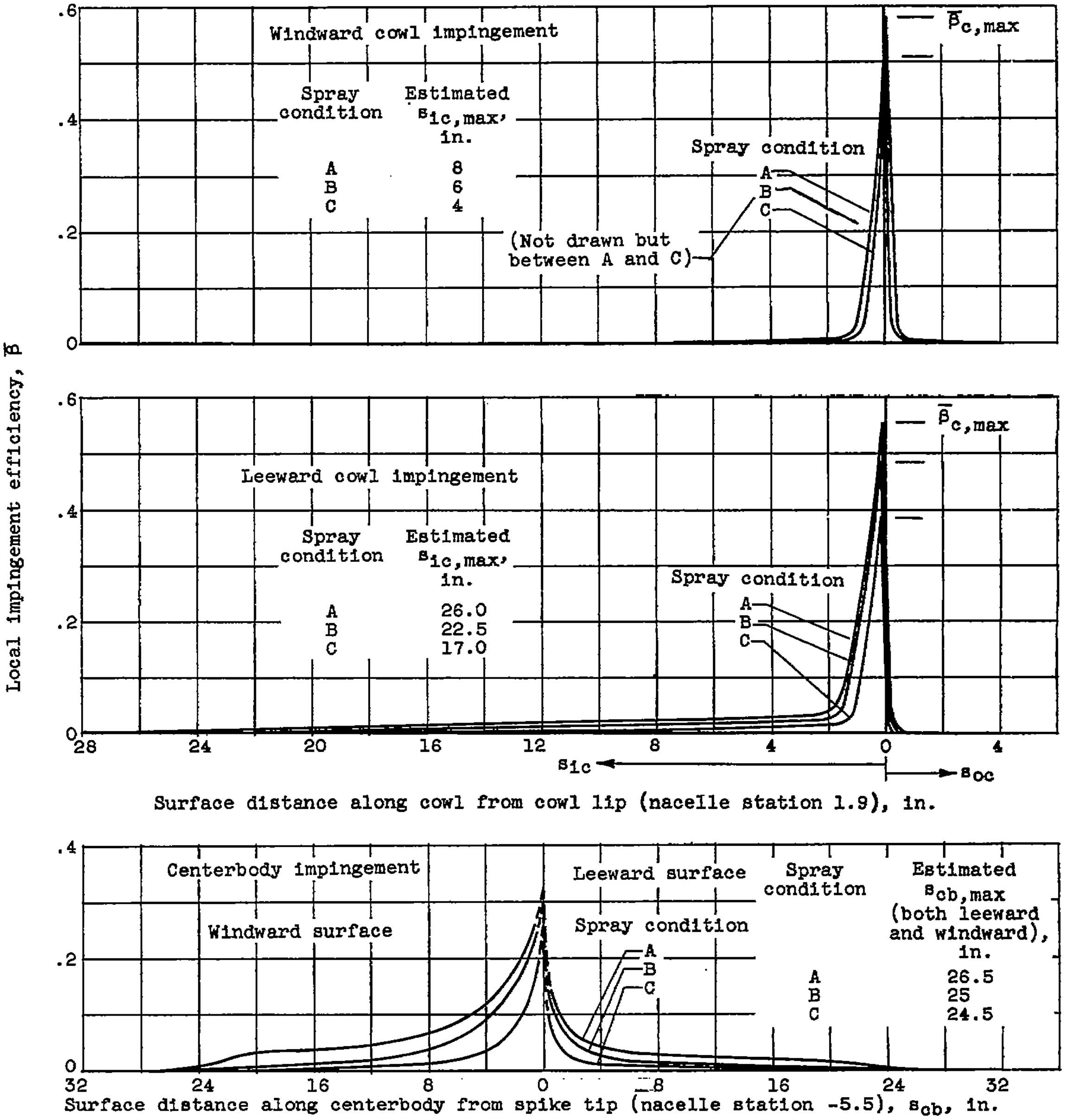

(b) Inlet velocity ratio, 0.680.

Figure 6. - Continued. Local impingement efficiency of cowl and centerbody of supersonic-nose-inlet model. Angle of attack, 4.2°.

4704

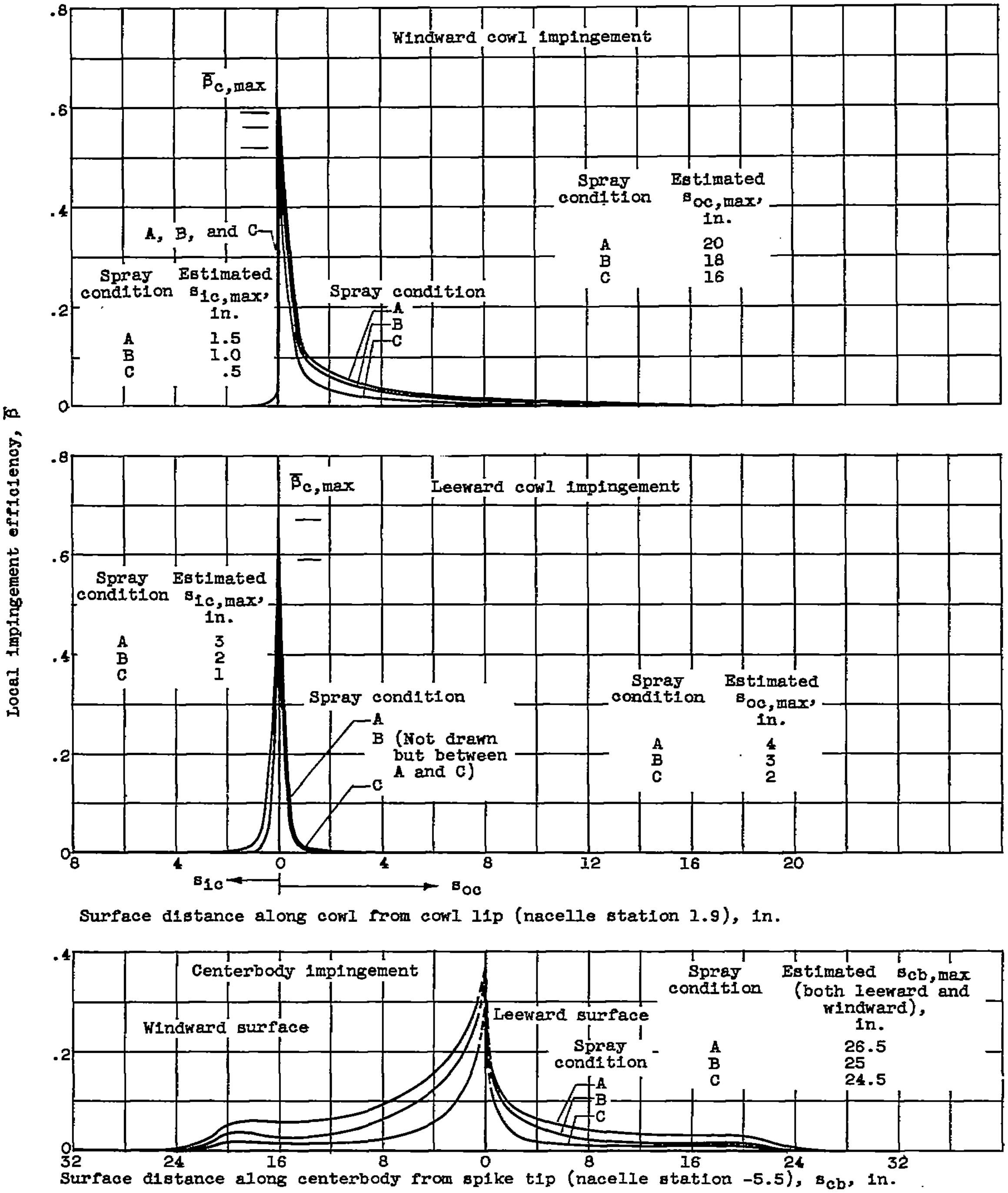

(c) Inlet velocity ratio, 1.294.

Figure 6. - Continued. Local impingement efficiency of cowl and centerbody of supersonic-nose-inlet model. Angle of attack, 4.2°.

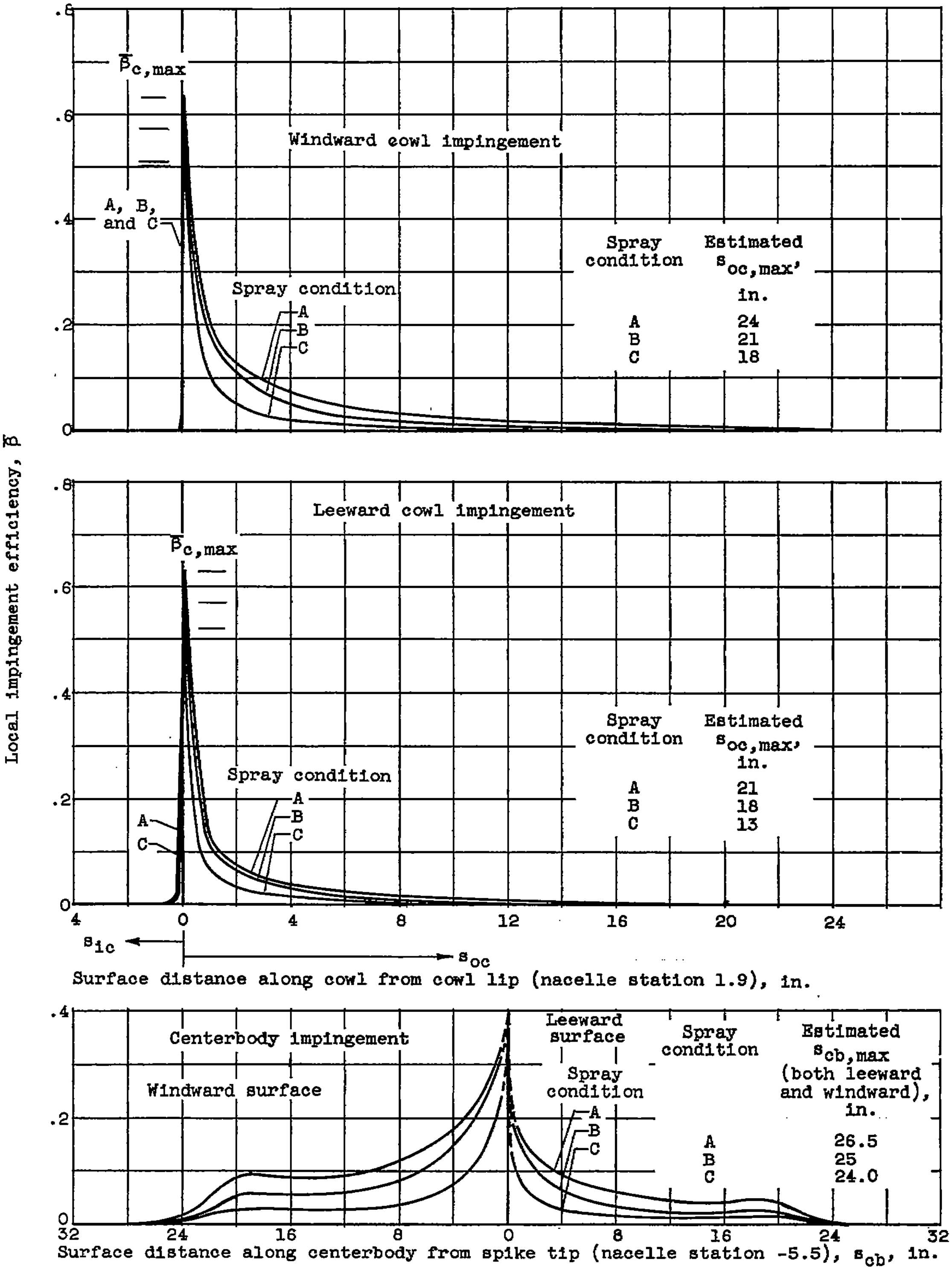

(d) Inlet velocity ratio, 1.771.

Figure 6. - Concluded. Local impingement efficiency of cowl and centerbody of supersonic-nose-inlet model. Angle of attack, 4.2°.

4704

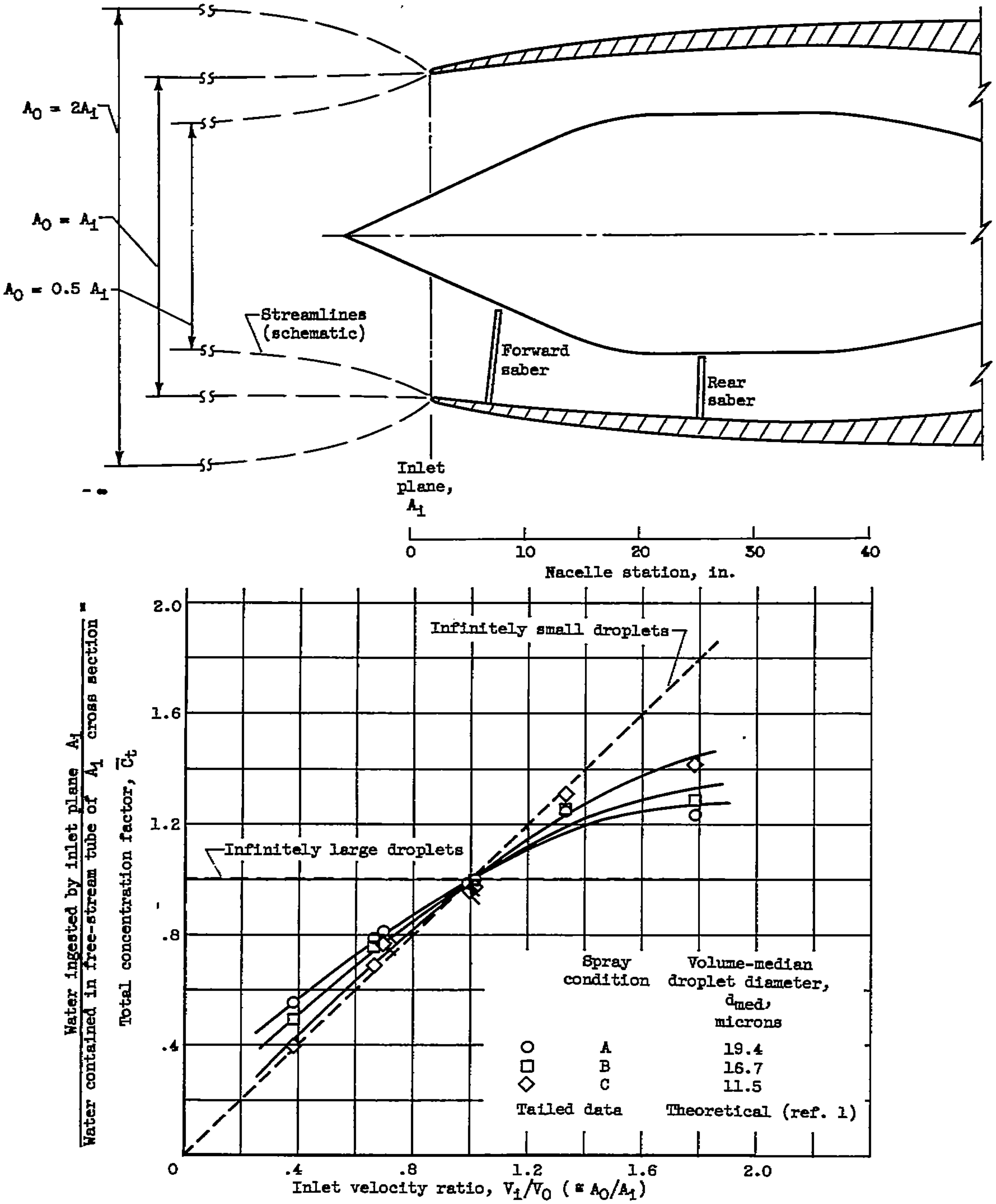

Figure 7. - Total concentration factor (scooping ratio) of supersonic-nose-inlet model as function of inlet velocity ratio. Angle of attack, 0°.

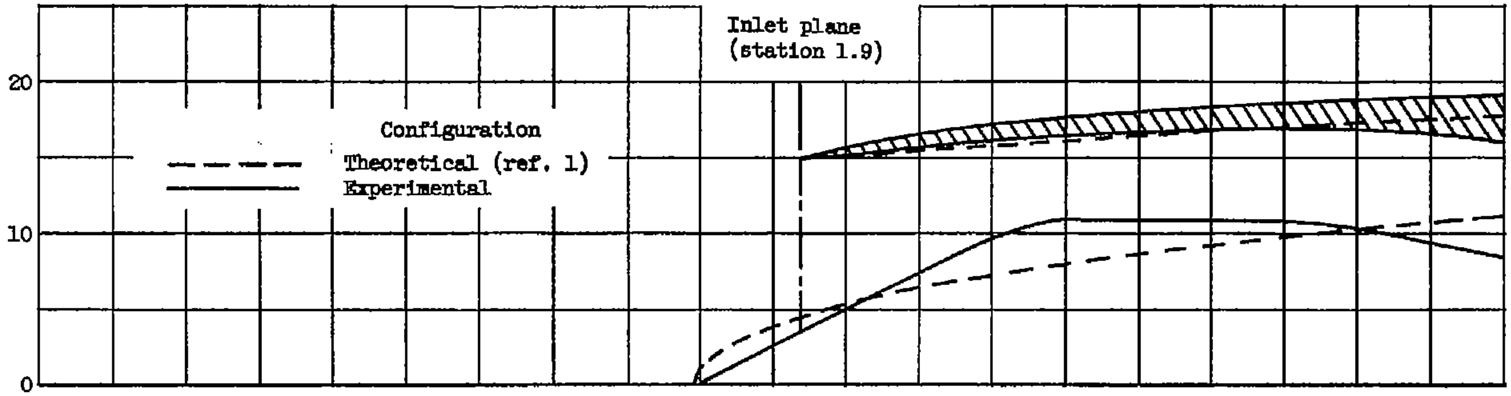

(a) Inlet velocity ratio, 1.0.

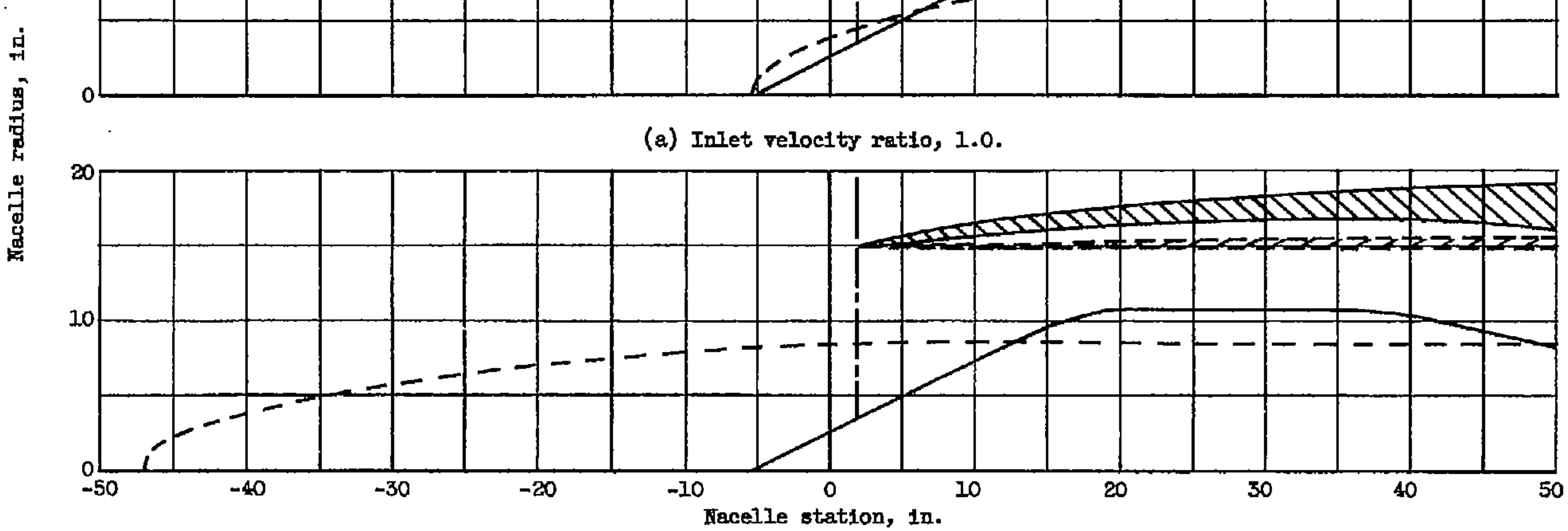

(b) Inlet velocity ratio, 0.7.

Figure 8. - Schematic geometric comparison of experimental inlet configuration with theoretically studied configurations.

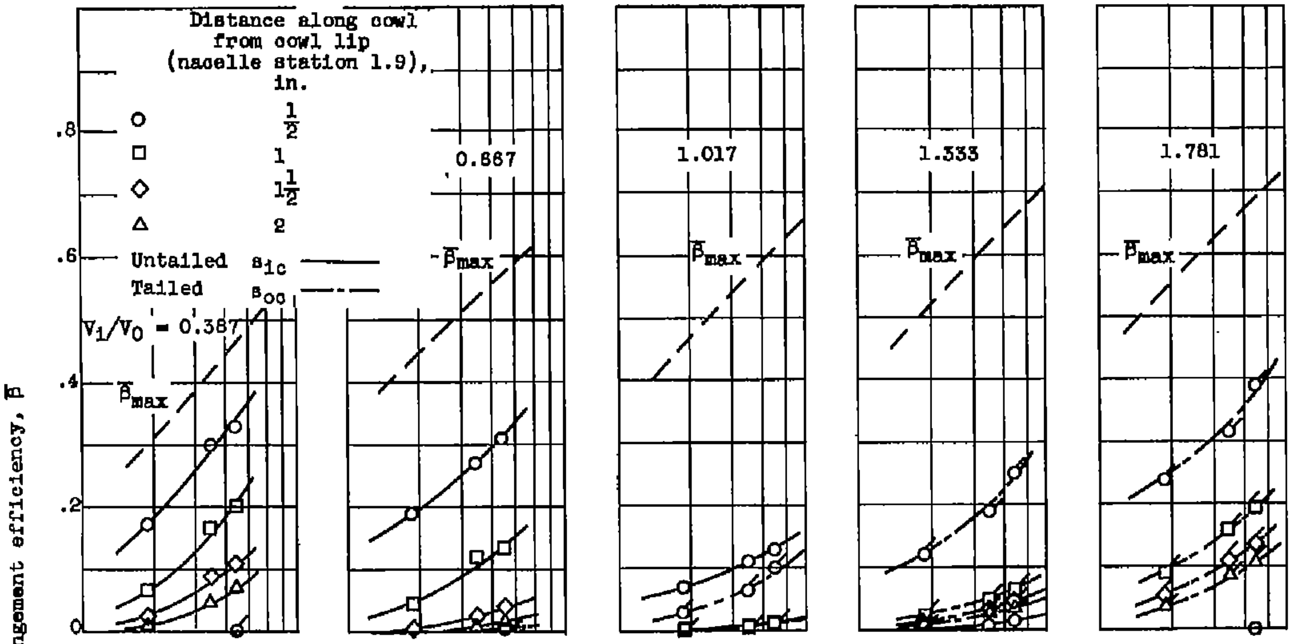

(a) Cowl impingement.

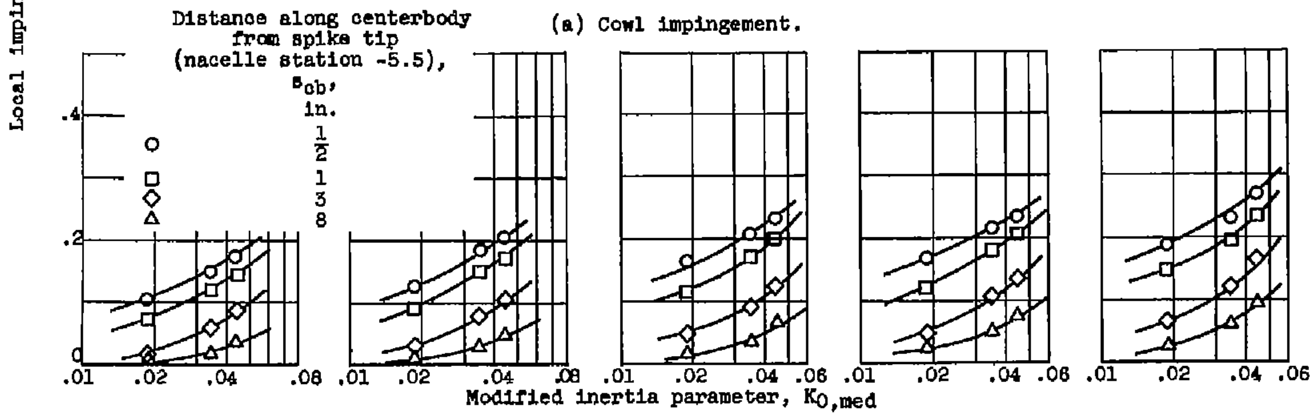

(b) Conical centerbody impingement.

Figure 9. - Local impingement efficiency of cowl and centerbody of supersonic-nose-inlet model as function of modified inertia parameter and inlet velocity ratio. Angle of attack, 0°.

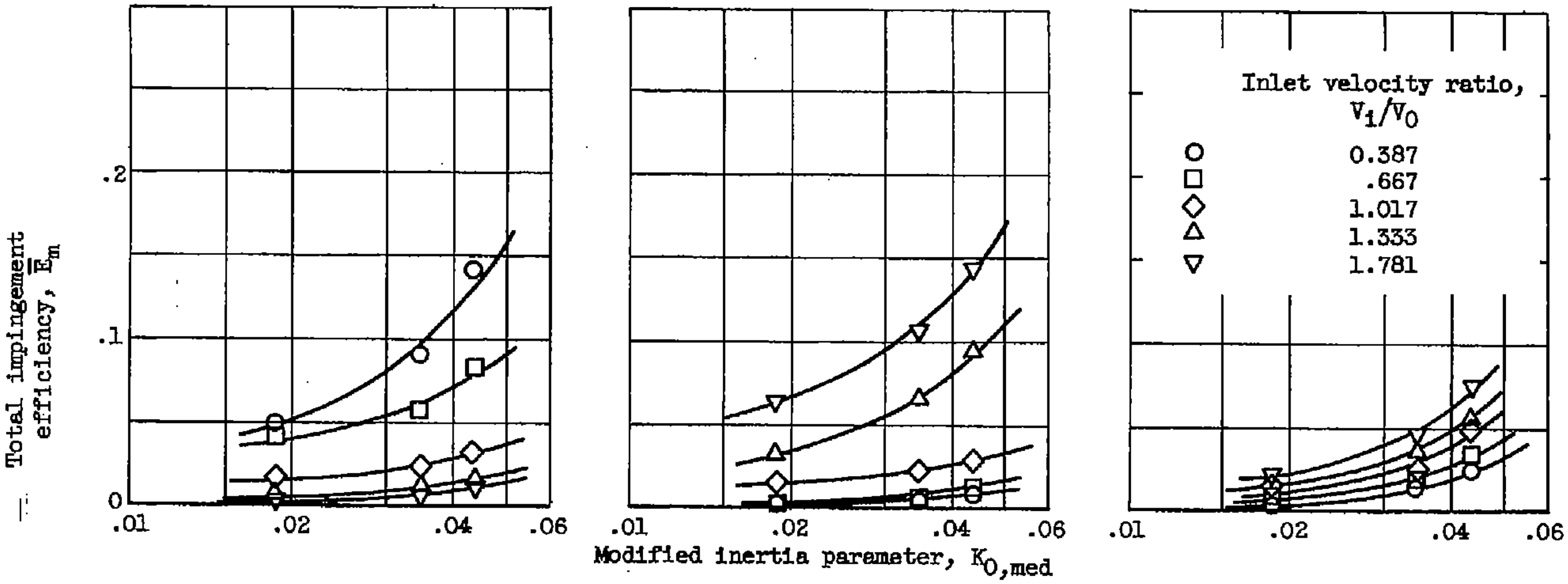

(a) Inner cowl.

(b) Outer cowl.

(c) Centerbody.

Figure 10. - Total impingement efficiencies of supersonic-nose-inlet components as function of modified inertia parameter and inlet velocity ratio. Angle of attack, 0°.

4704

CQ-7 back

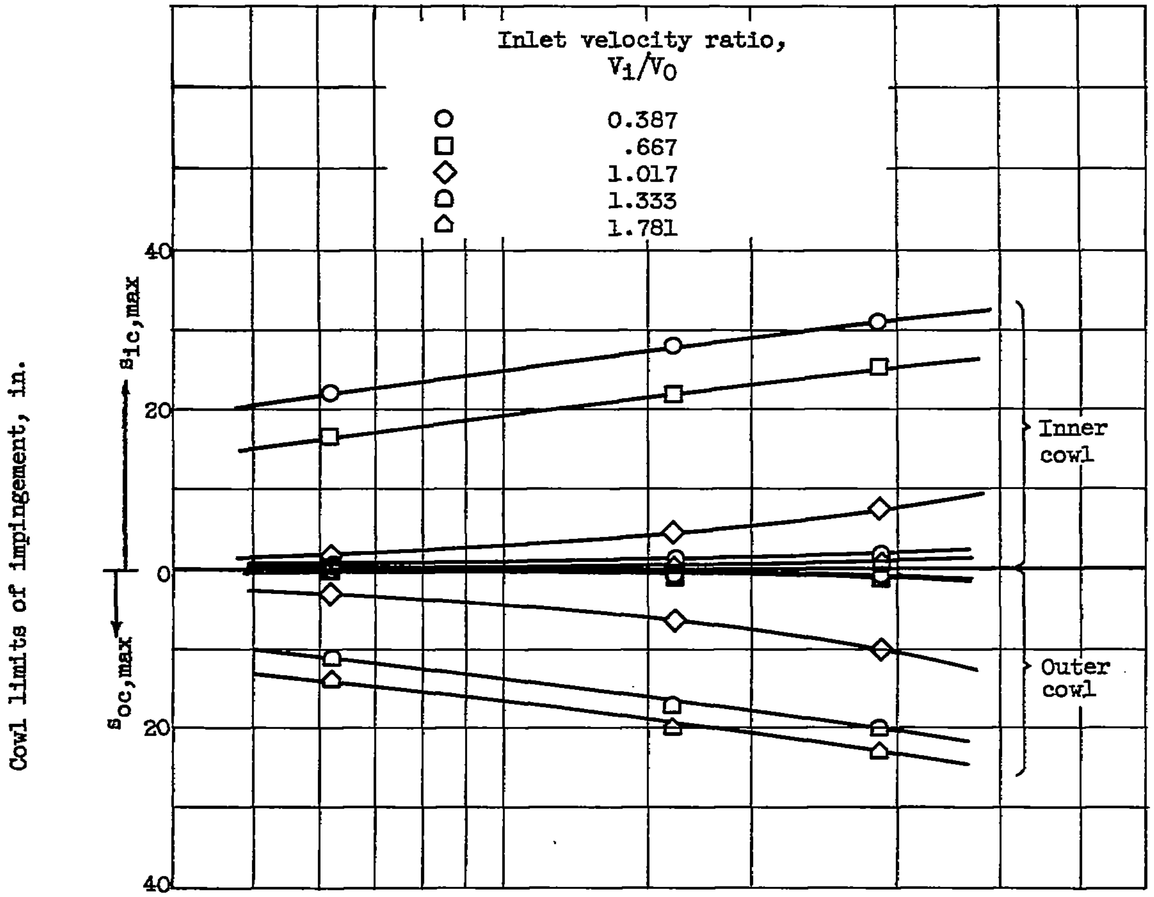

(a) Cowl limits of impingement.

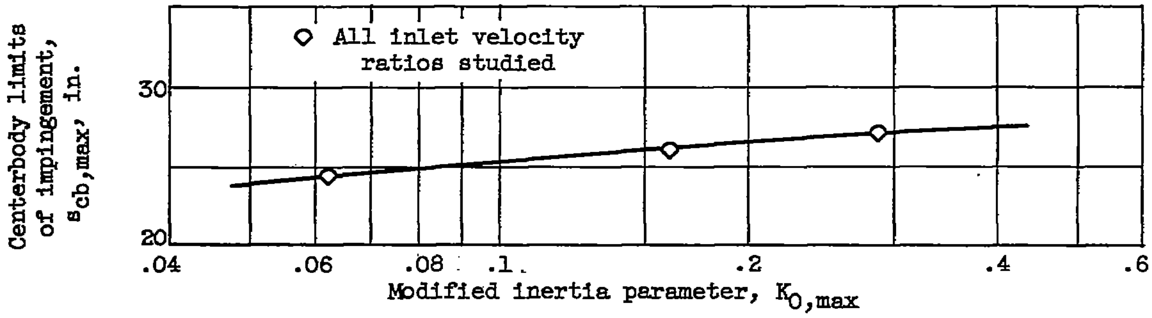

(b) Conical centerbody limits of impingement.

Figure 11. - Limits of impingement on cowl and centerbody of supersonic-nose-inlet model as function of modified inertia parameter and inlet velocity ratio. Angle of attack, 0°.

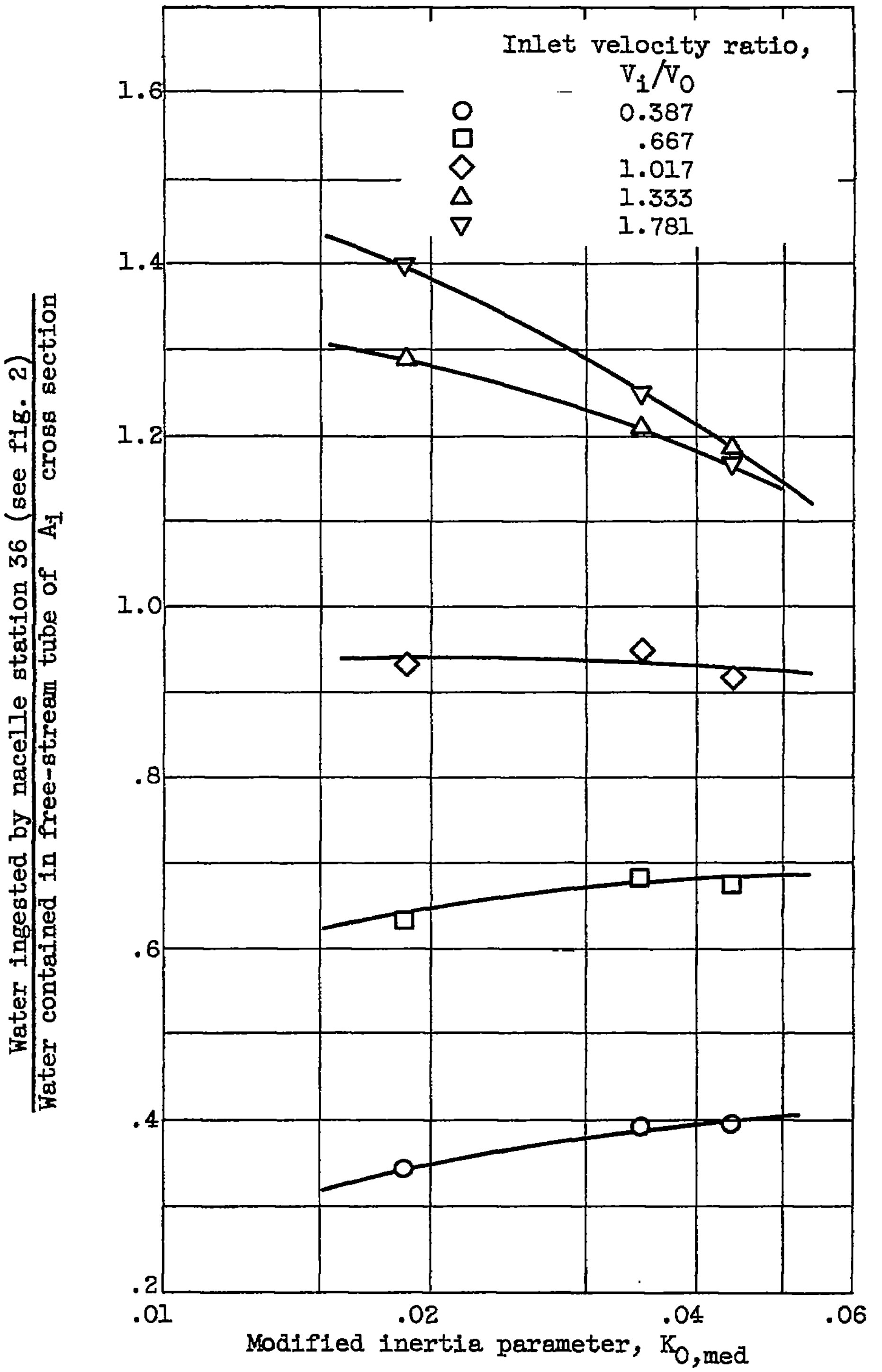

Figure 12. - Unimpinged water ingested by supersonic-nose-inlet model as function of modified inertia parameter and inlet velocity ratio. Angle of attack, 0°.

4704

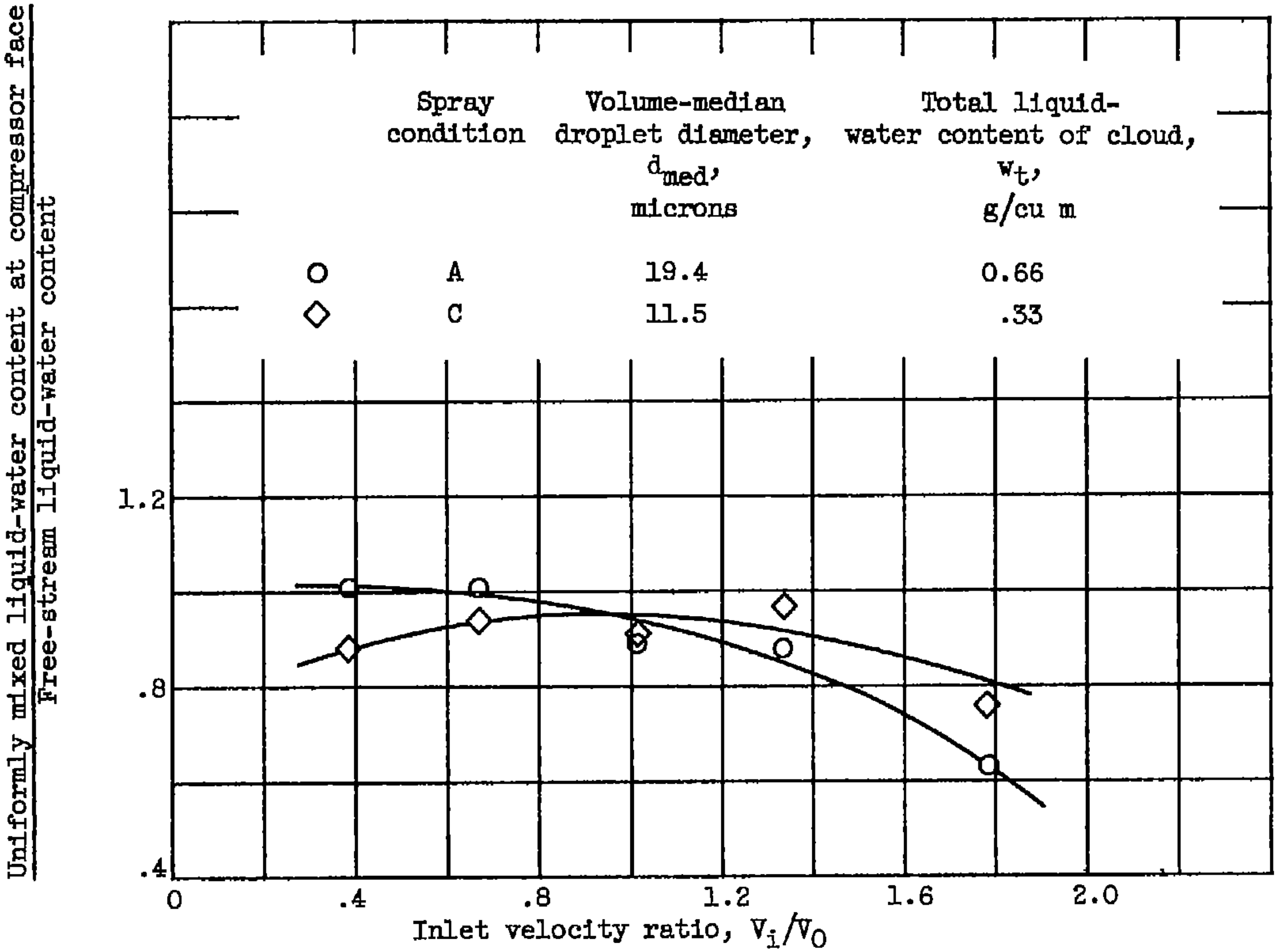

Figure 13. - Liquid-water content at compressor-face (nacelle station 85) ratio to free stream. Supersonic-nose-inlet model at zero angle of attack.

4704

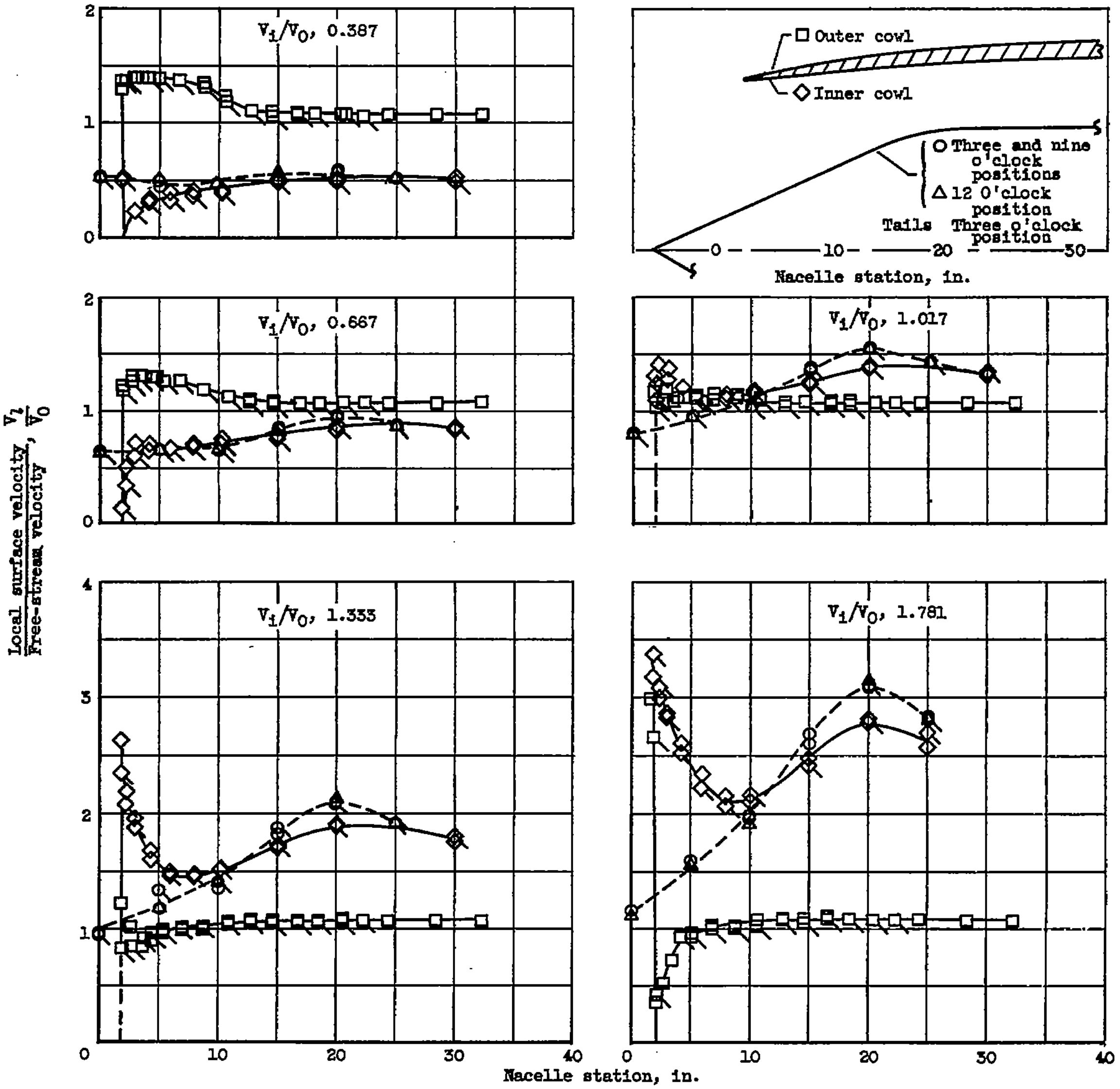

(a) Angle of attack, 0°.

Figure 14. - Local surface to free-stream velocity ratios of centerbody and cowl of inlet model.

4704

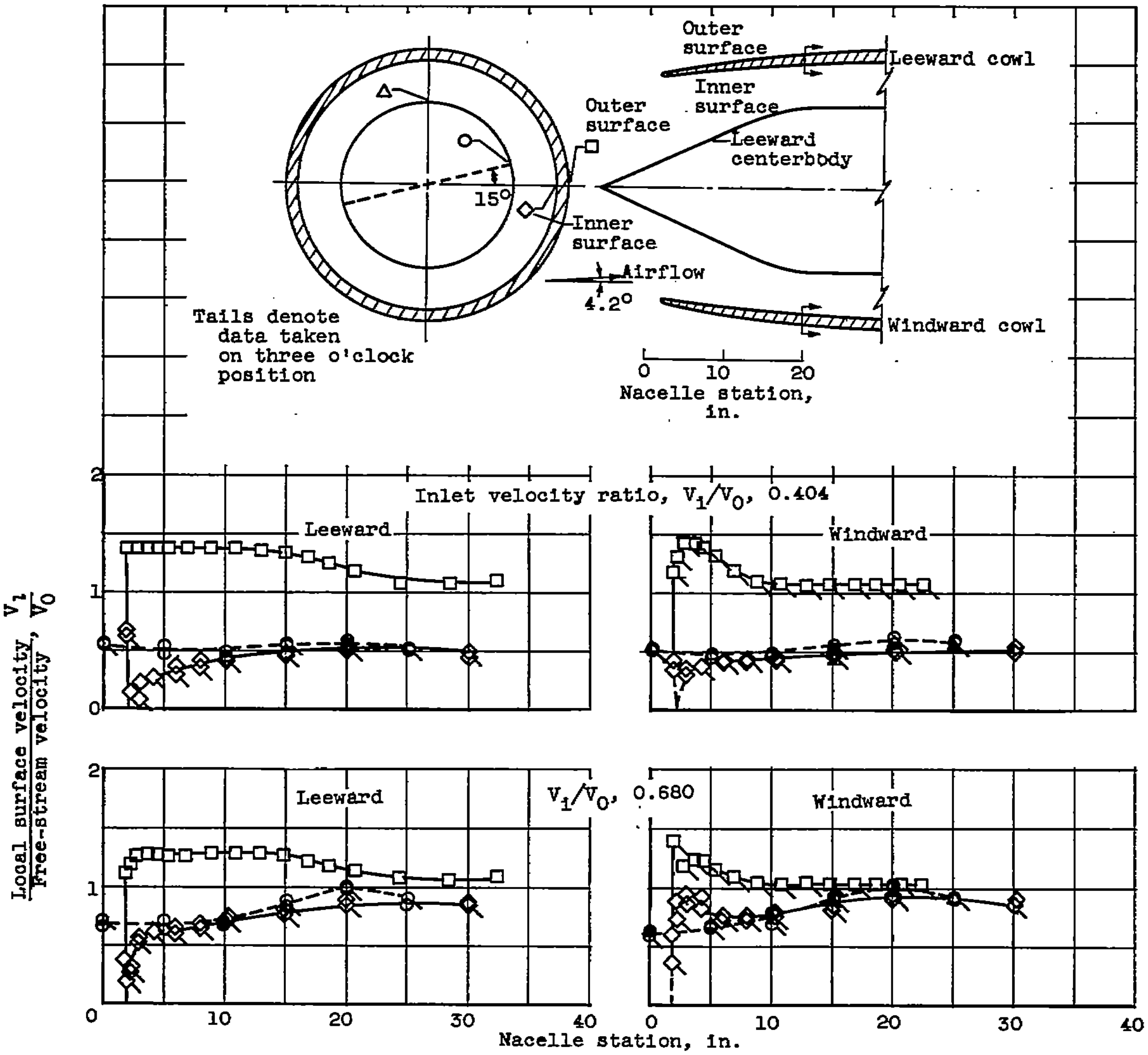

(b) Angle of attack, 4.2°.

Figure 14. - Continued. Local surface to free-stream velocity ratios of centerbody and cowl of inlet model.

4704

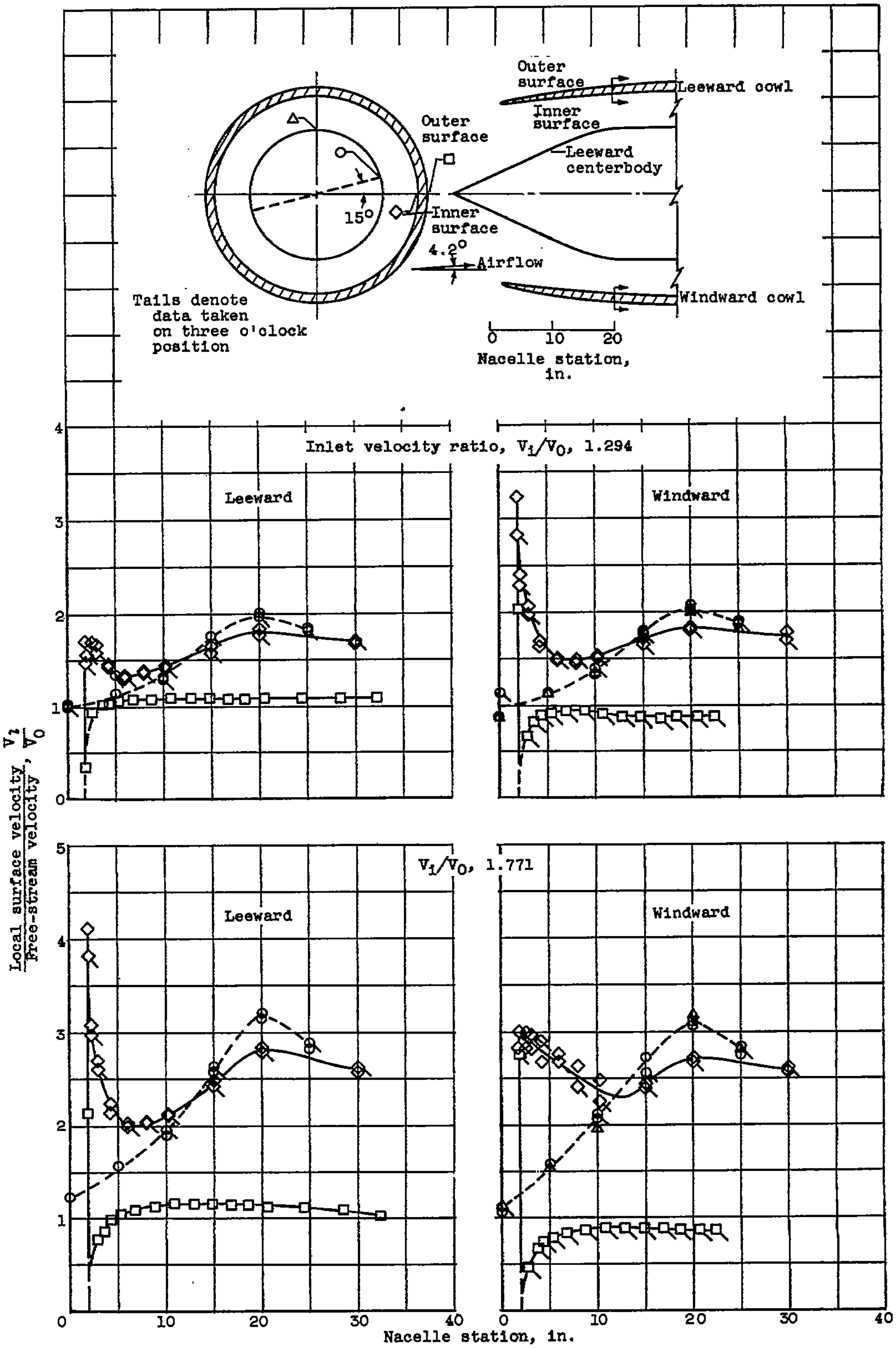

(b) Concluded. Angle of attack, 4.2°.

Figure 14. - Concluded. Local surface to free-stream velocity ratios of centerbody and cowl of inlet model.

NACA - Langley Field, Va.